Supporting Information to accompany:

Entropic Separation of Styrene/Ethylbenzene Mixtures by Exploitation of Subtle Differences in Molecular Configurations in Ordered Crystalline Nanoporous Adsorbents

Ariana Torres-Knoop[1], Jurn Heinen, Rajamani Krishna, and David Dubbeldam
Van 't Hoff Institute for Molecular Sciences, University of Amsterdam,
Science Park 904, 1098XH, Amsterdam, The Netherlands

March 2, 2015

[1]email: A.TorresKnoop@uva.nl

1 Adsorption isotherms

To compute the adsorption isotherms we performed Monte Carlo simulations in the grand-canonical ensemble (or μ, V, T ensemble). In this ensemble, the temperature T, the volume V, and the chemical potential μ are fixed. The Metropolis algorithm is implemented in the same way as for NVT ensemble, but in this case also the number of adsorbates is allowed to change by having an insertion and a deletion move. The number of adsorbates will fluctuate until equilibrium conditions are reached: the temperature and chemical potential of the gas inside and outside the adsorbent are equal. The imposed chemical potential is related to the fugacity f by

$$\beta\mu = \beta\mu^0_{\mathrm{id}} + \ln(\beta f), \tag{1.1}$$

where μ^0_{id} is the reference chemical potential and β the inverse of temperature.

Because in confined systems the fraction of successful insertions and deletions is very low, reaching equilibrium with conventional Monte Carlo methods can be very time consuming. In this study we use the Configurational Bias Continuous Fractional Monte Carlo (CB/CFCMC) [1] method to enhance the success rate of insertions and deletions. The method is a combination of the Configurational Bias Monte Carlo (CBMC)[2, 3, 4], where molecular growth is biased towards favorable configurations and Continuous Fractional Component Monte Carlo (CFCMC) [5] in which molecules are gradually inserted or deleted by scaling their intermolecular interactions with the surroundings using a parameter λ. In this method, new molecules are inserted and old chains are removed using configurational biasing at constant λ values and λ is changed by using $\lambda(n) = \lambda(o) + \epsilon$, where ϵ is chosen uniformly between $-\Delta\lambda^{\max}$ and $+\Delta\lambda^{\max}$ and adjusted to achieve approximately 50% acceptance. Because many systems show behavior where λ-changes are difficult [5, 6, 7], an additional bias η on λ can be used which is afterwards removed by the acceptance rules. When $\lambda = 0$ or $\lambda = 0 = 1$ the algorithm reduces to conventional CBMC for insertion and deletion, respectively. We have shown in previous work[1] that the results obtain with this method do not differ from CBMC calculations but the efficiency is higher. The acceptance rules for insertion and deletion are given by:

- Insertion move, $\lambda_n = 1 + \epsilon$
  A new fractional molecule with $\lambda_n = \epsilon$ is grown at a random position using CBMC giving $W(n)$.

$$\mathrm{acc}\,(\mathrm{o} \to \mathrm{n}) = \min\left(1, \frac{f\beta V}{N+1}\frac{W(n)}{\langle W^{\mathrm{IG}}\rangle}\exp[-\beta\Delta U]\exp[\eta(\lambda(n)) - \eta(\lambda(o))]\right) \tag{1.2}$$

- Deletion move, $\lambda_n = -\epsilon$
  The existing fractional particle is retraced using CBMC with $\lambda = \lambda_o$ giving W(o) and the fractional molecule is subsequently removed.

$$\mathrm{acc}\,(\mathrm{o} \to \mathrm{n}) = \min\left(1, \frac{N}{f\beta V}\frac{\langle W^{\mathrm{IG}}\rangle}{W(o)}\exp[-\beta\Delta U]\exp[\eta(\lambda(n)) - \eta(\lambda(o))]\right) \tag{1.3}$$

Together with insertion and deletion moves, several types of Monte Carlo moves are employed during a simulation to thermalize the system:

- Displacement move
  A molecule is selected at random and given a random displacement. The maximum displacement is taken such that 50% of the moves is accepted. The acceptance rule is

$$\mathrm{acc}\left(\mathrm{o} \rightarrow \mathrm{n}\right) = \min\left(1, e^{-\beta\left(U^{\mathrm{n}} - U^{\mathrm{o}}\right)}\right). \tag{1.4}$$

  Note that the energy of the new configuration U^{n} and the energy of the old configuration U^{o} only differ in the external energy.

- Rotation move
  A molecule is selected at random and given a random rotation. The center of the rotation is the center of mass. The maximum rotation angle is selected such that 50% of the moves are accepted. The acceptance rule is given by Eq. 1.4. Again, the energy of the new configuration U^{n} and the energy of the old configuration U^{o} only differ in the external energy.

- Identity change move (mixtures)
  The identity-change trial move [8] is called semi-grand ensemble, but it can also be seen as a special case of the Gibbs ensemble. One of the components is selected at random and an attempt is made to change its identity. The acceptance rule is given by [9]

$$\mathrm{acc}\left(\mathrm{A} \rightarrow \mathrm{B}\right) = \min\left(1, \frac{W^{\mathrm{new}} f_B \left\langle W_A^{\mathrm{IG}} \right\rangle N_A}{W^{\mathrm{old}} f_A \left\langle W_B^{\mathrm{IG}} \right\rangle \left(N_B + 1\right)}\right), \tag{1.5}$$

  where f_A and f_B are the fugacities of components A and B, and N_A and N_B are the number of particles.

Simulations are performed in cycles. The number of cycles needed for equilibration depends on the number of molecules. We define a cycle to consists of smaller steps proportional to the number number of molecules with 20 as the minimum.

$$N_{\mathrm{cycles}} = \max\left(20, N\right) \times N_{\mathrm{steps}}. \tag{1.6}$$

In each step one Monte Carlo move is performed. For the isotherms we used at least 500000 initialization cycles, while 500000 cycles are used to compute the isotherms. The error bars in the isotherms are computed by dividing the simulations results up into five blocks. The error is computed from the standard deviation of the five blocks and corresponds to the 95% confidence interval.

2
Case Studies

2.1 MFI-para: size exclusion

2.1.1 Snapshots

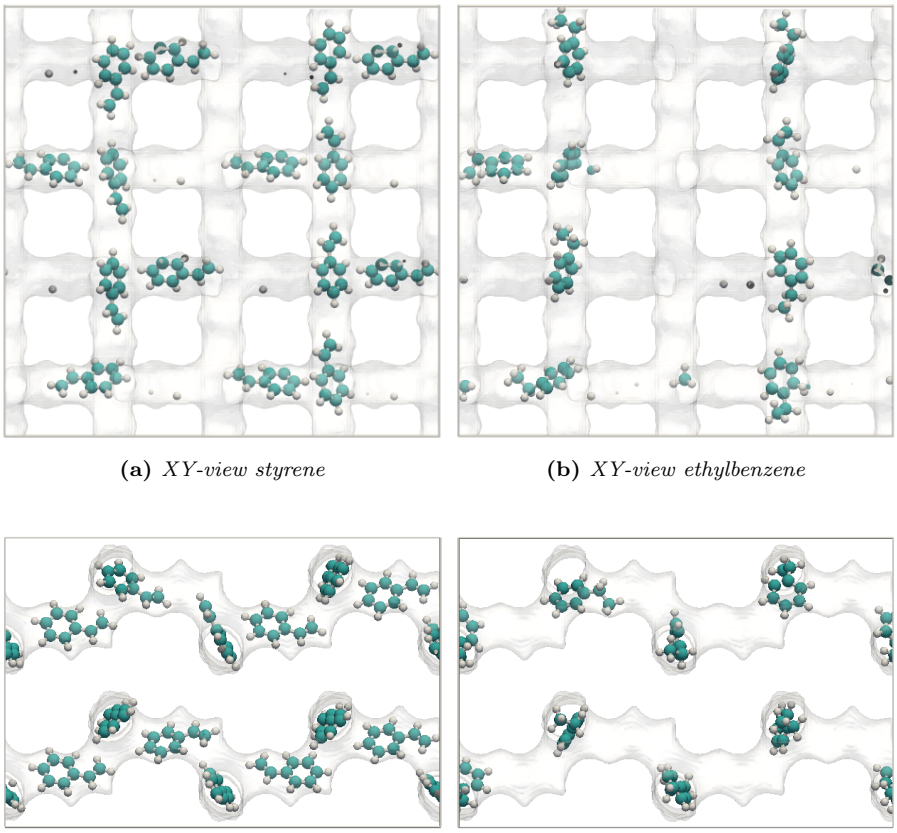

(a) *XY-view styrene* **(b)** *XY-view ethylbenzene*

(c) *XZ-view styrene* **(d)** *XZ-view ethylbenzene*

Figure S1: *Snapshots of styrene and ethylbenzene in MFI-para at 433K and 1e9Pa. Styrene can be adsorbed in the straight and the zig-zag channels but ethylbenzene positions in the zig-zag channels are hindered by the ones in the intersections The size exclusion effect in the zig-zag channels causes a significant difference in the saturation capacities of both molecules. MFI-para is a styrene selective structure at saturation capacity. Color code: carbon (cyan), hydrogen (white).*

2.1.2 Langmuir-Freundlich parameters

	site A			site B		
	$q_{i,A,\text{sat}}$ [mol kg^{-1}]	$b_{i,A}$ [Pa$^{-\nu_{i,A}}$]	$\nu_{i,A}$ [-]	$q_{i,B,\text{sat}}$ [mol kg^{-1}]	$b_{i,B}$ [Pa$^{-\nu_{i,B}}$]	$\nu_{i,B}$ [-]
styrene	0.61	1.41×10^{-5}	1.1	0.6	1.61×10^{-7}	1.03
ethylbenzene	0.14	4.95×10^{-6}	1.05	0.57	1.96×10^{-7}	1.15

Table S1: *Dual-site Langmuir-Freundlich parameters for pure component styrene and ethylbenzene isotherms at 433K in MFI-para.*

2.1.3 Adsorption isotherms

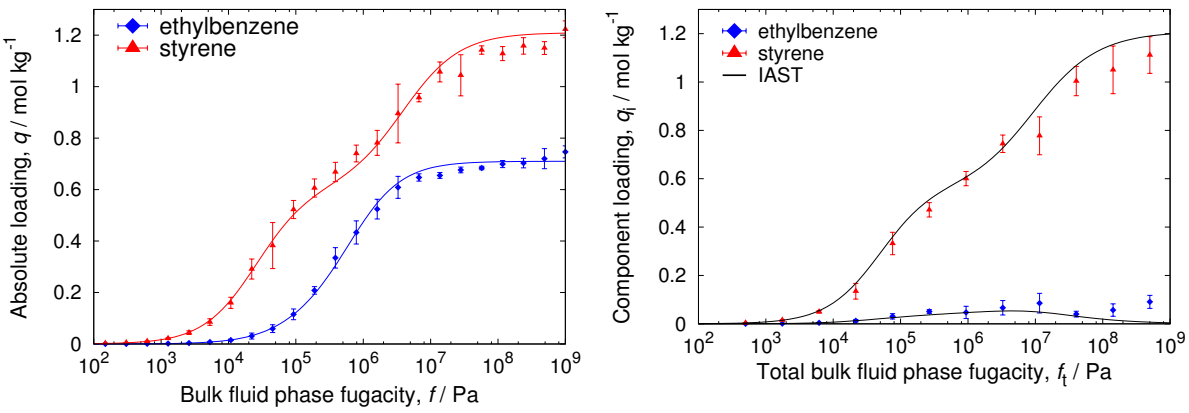

(a) (b)

Figure S2: *Simulated isotherms of styrene and ethylbenzene in MFI-para at 433K. (a) Pure component isotherms (lines are dual-site Langmuir-Freundlich fits of the pure components, points are the pure component isotherms from CB/CFCMC simulations) (b) mixture component isotherms for an equimolar mixture.The IAST results are in good agreement with the mixture isotherms.*

2.1.4 Breakthrough simulations

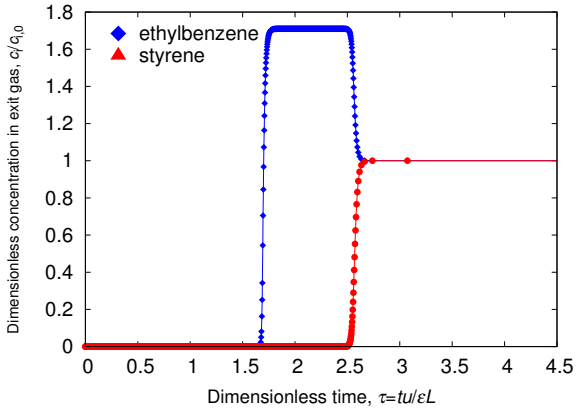

Figure S3: *Simulated step-type breakthrough curves of an equimolar mixture of styrene and ethylbenzene in MFI-para at 433K and 1e6 Pa total fugacity. Video animations of the breakthrough behavior as a function of time are provided as Supplementary information.*

2.2 AFI: face-to-face stacking

2.2.1 Snapshots

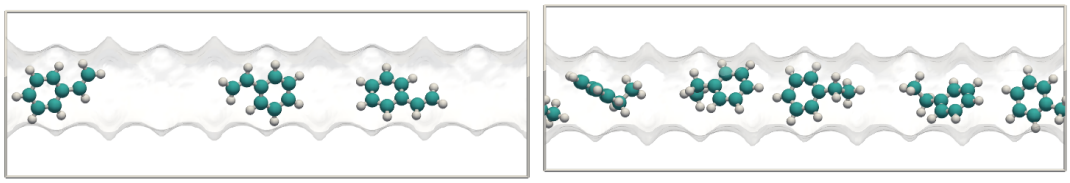

(a) *1e4 Pa*

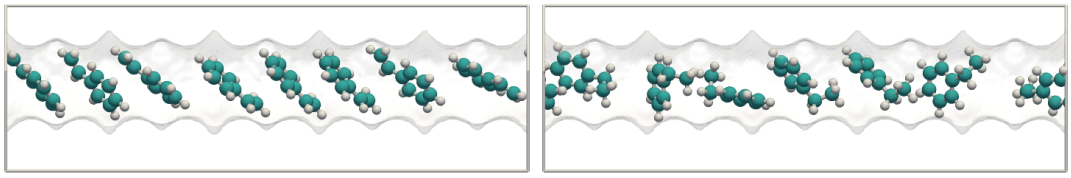

(b) *1e9 Pa*

Figure S4: *Snapshots of styrene (left) and ethylbenzene (right) in AFI zeolite at 433K and 1e4 Pa (top) and 1e9 Pa (bottom). At low loadings, molecules are preferentially adsorbed flat on the walls (parallel to the channel axis) to enhance their interactions. Ethylbenzene has stronger interactions with the framework under these conditions. At saturation loadings styrene undergoes a molecular reorientation into a face-to-face configuration. This reorientation reduces styrene's footprint in the channels allowing for more molecules to be adsorbed and a higher saturation capacity to be obtained. Ethylbenzene size does not allow for this reorientation to be completed. Color code: carbon (cyan), hydrogen (white).*

2.2.2 Langmuir-Freundlich parameters

	site A			site B		
	$q_{i,A,\text{sat}}$ [mol kg^{-1}]	$b_{i,A}$ [Pa$^{-\nu_{i,A}}$]	$\nu_{i,A}$ [-]	$q_{i,B,\text{sat}}$ [mol kg^{-1}]	$b_{i,B}$ [Pa$^{-\nu_{i,B}}$]	$\nu_{i,B}$ [-]
styrene	0.3	8.1×10^{-8}	1	0.8	1.23×10^{-4}	1
ethylbenzene	0.3	8.44×10^{-6}	0.74	0.67	1.45×10^{-4}	1.1

Table S2: *Dual-site Langmuir-Freundlich parameters for pure component styrene and ethylbenzene at 433K in AFI.*

2.2.3 Adsorption isotherms

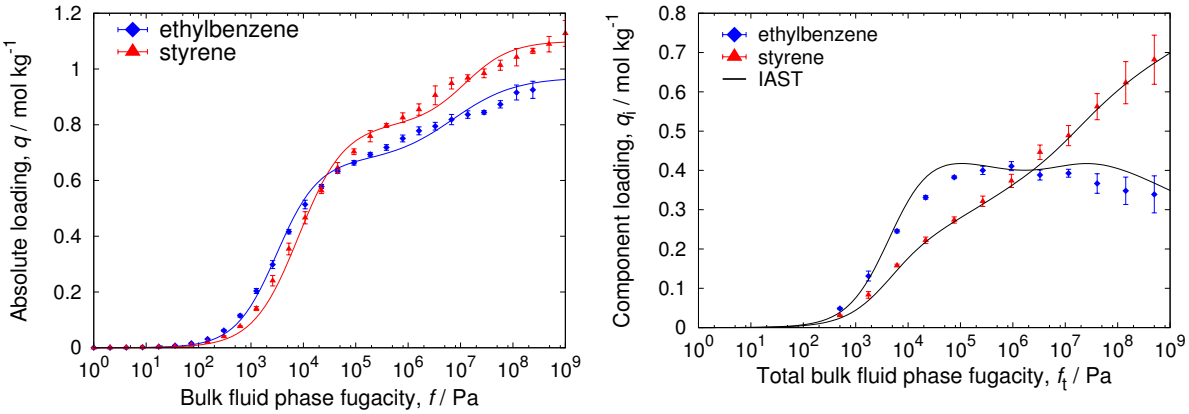

(a) **(b)**

Figure S5: *Simulated isotherm of styrene and ethylbenzene in AFI zeolite at 433K. (a) Pure component isotherms (lines are dual-site Langmuir-Freundlich fits of the pure components, points are the pure component isotherms from CB/CFCMC simulations) (b) mixture component isotherms for an equimolar mixture. The IAST results are in good agreement with the mixture isotherms*

2.2.4 Breakthrough simulations

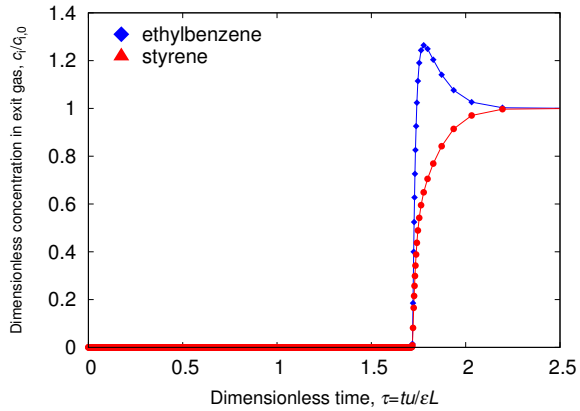

Figure S6: *Simulated step-type breakthrough of styrene and ethylbenzene in AFI at 433K and 1e6 Pa total fugacity. Video animations of the breakthrough behavior as a function of time are provided as Supplementary information.*

2.3 MAZ: face-to-face stacking

2.3.1 Snapshots

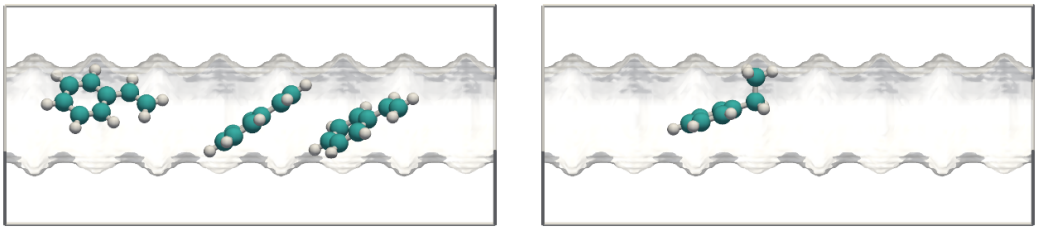

(a) *1e4 Pa*

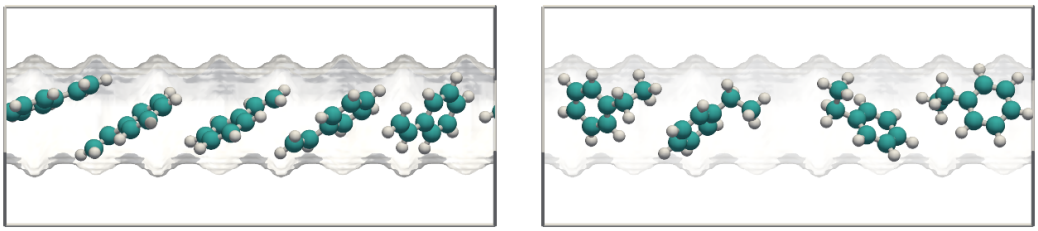

(b) *1e9 Pa*

Figure S7: *Snapshots of styrene (left) and ethylbenzene (right) in MAZ zeolite at 1e4 Pa (top) and 1e9 Pa (bottom) and 433K. MAZ zeolite has slightly smaller channels than AFI. The size of the channel determines how tilted the molecules have to be in a face-to-face stacking configuration and therefore it determines the molecule's footprint in the channel after reorientation. At low loadings, styrene adsorbs parallel to the channel axis, but MAZ channel's dimensions still make the reorientation into a face-to-face stacking configuration at high loadings favorable. Styrene footprint in the channels is reduced and a higher saturation capacity is obtain. For ethylbenzene, because of the non-planar ethyl group, a reorientation into face-to-face stacking does not reduce significantly the footprint of the molecule in the channels and therefore is not favorable. At saturation conditions MAZ is a styrene selective structure.*

2.3.2 Langmuir-Freundlich parameters

	site A			site B		
	$q_{i,A,\text{sat}}$ [mol kg^{-1}]	$b_{i,A}$ [Pa$^{-\nu_{i,A}}$]	$\nu_{i,A}$ [-]	$q_{i,B,\text{sat}}$ [mol kg^{-1}]	$b_{i,B}$ [Pa$^{-\nu_{i,B}}$]	$\nu_{i,B}$ [-]
styrene	0.2	6.8×10^{-6}	0.8	0.4	1.22×10^{-4}	1.05
ethylbenzene	0.12	3.89×10^{-6}	0.67	0.42	1.72×10^{-4}	1.02

Table S3: *Dual-site Langmuir-Freundlich parameters for pure component styrene and ethylbenzene at 433K in MAZ.*

2.3.3 Adsorption isotherms

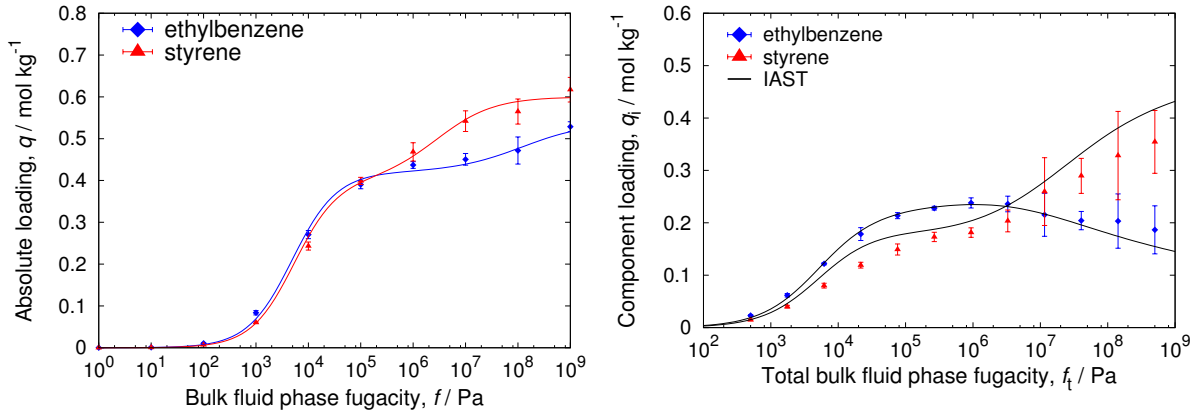

(a) **(b)**

Figure S8: *Simulated isotherms of styrene and ethylbenzene in MAZ at 433K. (a) Pure component isotherms (lines are dual-site Langmuir-Freundlich fits of the pure components, points are the pure component isotherms from CB/CFCMC simulations)(b) mixture component isotherms for an equimolar mixture. The IAST results are in good agreement with the mixture isotherms*

2.3.4 Breakthrough simulations

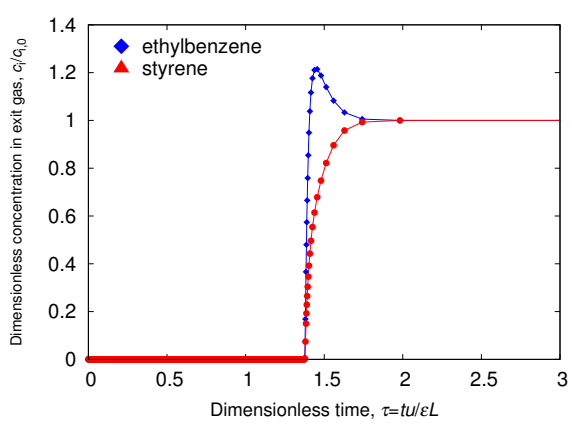

Figure S9: *Simulated step-type breakthrough of styrene and ethylbenzene in AFI at 433K and 1e6 total fugacity. Video animations of the breakthrough behavior as a function of time are provided as Supplementary information.*

2.4 DON: styrene commensurate stacking and ethylbenzene face-to-face stacking

2.4.1 Snapshots

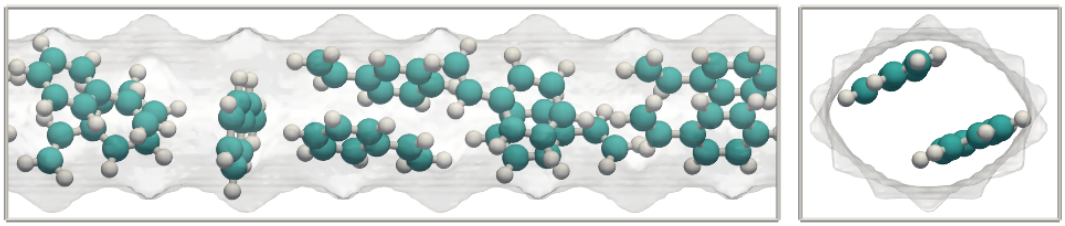

(a) *Styrene*

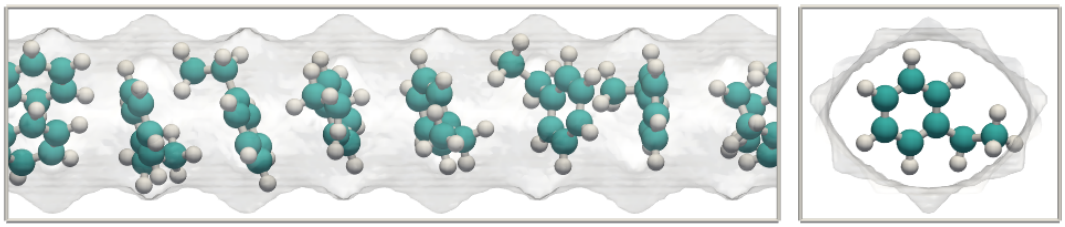

(b) *Ethylbenzene*

Figure S10: *Snapshots of styrene (top) and ethylbenzene (bottom) in DON zeolite at 1e9Pa and 433K. DON zeolite has larger channels than AFI and MAZ. Because of that, ethylbenzene can also undergo a reorientation into face-to-face stacking configuration that reduces its footprint in the channel. The channel dimensions however are also large enough for styrene to have commensurate stacking. Commensurate stacking allows styrene to obtain a higher saturation capacity than the one obtained by ethylbenzene in a face-to-face stacking configuration. Color code: carbon (cyan), hydrogen (white).*

2.4.2 Langmuir-Freundlich parameters

	site A			site B		
	$q_{i,A,\text{sat}}$ [mol kg^{-1}]	$b_{i,A}$ [Pa$^{-\nu_{i,A}}$]	$\nu_{i,A}$ [-]	$q_{i,B,\text{sat}}$ [mol kg^{-1}]	$b_{i,B}$ [Pa$^{-\nu_{i,B}}$]	$\nu_{i,B}$ [-]
styrene	0.2	8.75×10^{-7}	0.9	0.9	3.54×10^{-5}	1.1
ethylbenzene	0.3	3.64×10^{-6}	0.8	0.75	6.61×10^{-5}	1.1

Table S4: *Dual-site Langmuir-Freundlich parameters for pure component styrene and ethylbenzene at 433K in DON.*

2.4.3 Adsorption isotherms

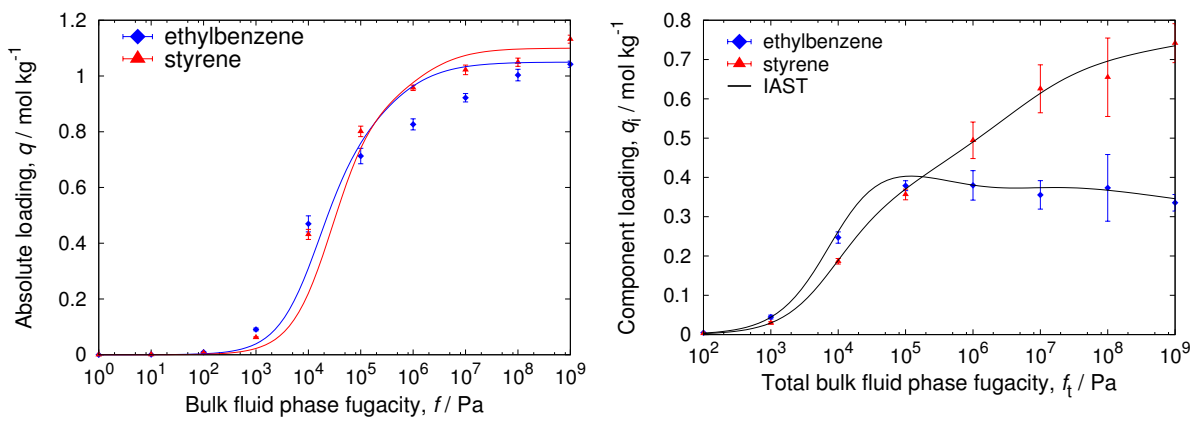

(a) **(b)**

Figure S11: *Simulated isotherms of styrene and ethylbenzene in DON zeolite at 433K. (a) Pure component isotherms (lines are dual-site Langmuir-Freundlich fits of the pure components, points are the pure component isotherms from CB/CFCMC simulations) (b) mixture component isotherms for an equimolar mixture. The IAST results are in good agreement with the mixture isotherms*

2.4.4 Breakthrough simulations

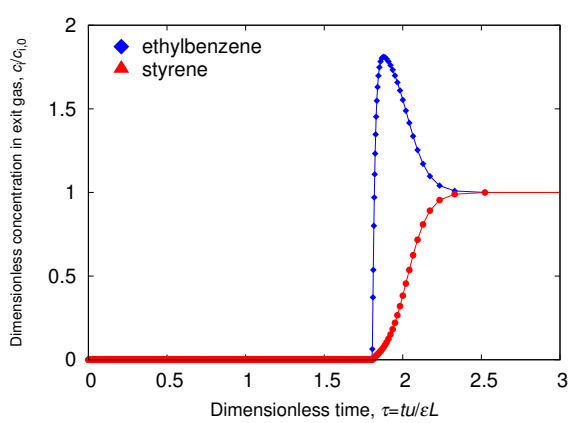

Figure S12: *Simulated step-type breakthrough of styrene and ethylbenzene in DON at 433K and 1e6 Pa total fugacity. Video animations of the breakthrough behavior as a function of time are provided as Supplementary information.*

2.5 MIL-53: styrene commensurate stacking and ethylbenzene face-to-face stacking

2.5.1 Snapshots

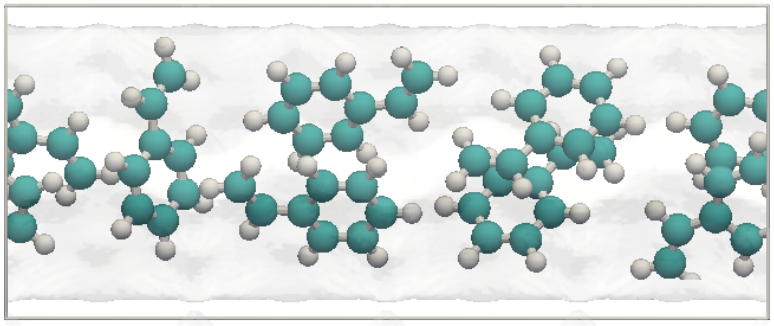

(a) *XZ-view styrene*

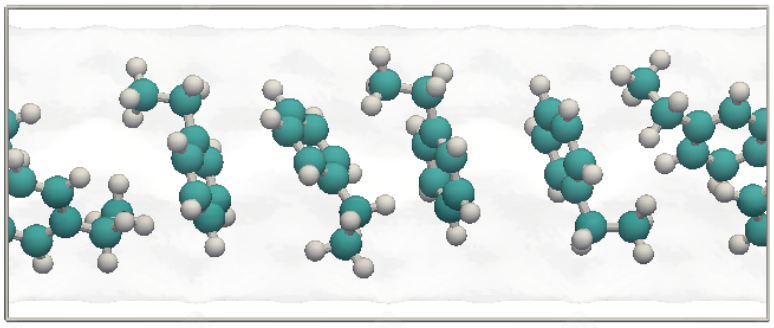

(b) *XZ-view ethylbenzene*

Figure S13: *Snapshots of styrene (top) and ethylbenzene (bottom) in MIL-53 at 1e9 Pa and 433K. Ethylbenzene has a face-to-face stacking configuration while styrene has commensurate stacking. Color code: carbon (cyan), hydrogen (white).*

2.5.2 Langmuir-Freundlich parameters

	site A			site B		
	$q_{i,A,\text{sat}}$ [mol kg^{-1}]	$b_{i,A}$ [Pa$^{-\nu_{i,A}}$]	$\nu_{i,A}$ [-]	$q_{i,B,\text{sat}}$ [mol kg^{-1}]	$b_{i,B}$ [Pa$^{-\nu_{i,B}}$]	$\nu_{i,B}$ [-]
styrene	1.33	7.15×10^{-4}	0.66	2	3.74×10^{-3}	1.07
ethylbenzene	0.73	5.41×10^{-5}	0.73	2.2	6.6×10^{-3}	1

Table S5: *Dual-site Langmuir-Freundlich parameters for pure component styrene and ethylbenzene at 433K in MIL-53.*

2.5.3 Adsorption isotherms

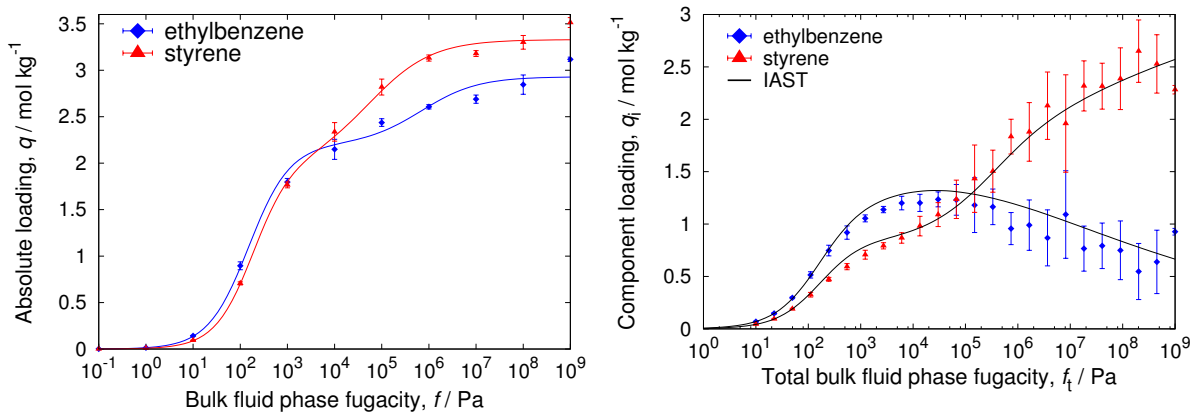

(a) (b)

Figure S14: *Simulated isotherms of styrene and ethylbenzene in MIL-53 at 433K. (a) Pure component isotherms (lines are dual-site Langmuir-Freundlich fits of the pure components, points are the pure component isotherms from CB/CFCMC simulations) (b) mixture component isotherms for an equimolar mixture. The IAST results are in good agreement with the mixture isotherms*

2.5.4 Breakthrough simulations

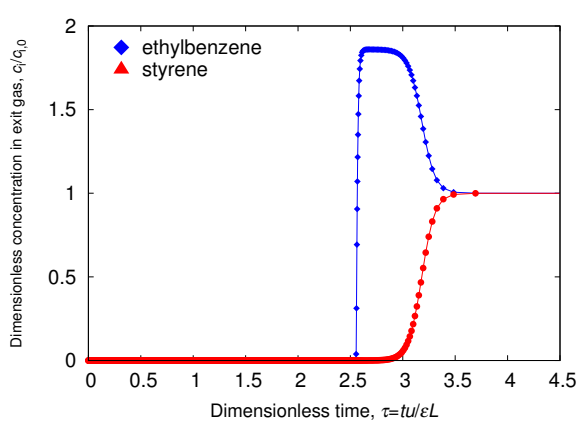

Figure S15: *Simulated step-type breakthrough of styrene and ethylbenzene in MIL-53 at 433K and 1e6 Pa total fugacity. Video animations of the breakthrough behavior as a function of time are provided as Supplementary information.*

2.6 MIL-47: commensurate stacking

2.6.1 Snapshots

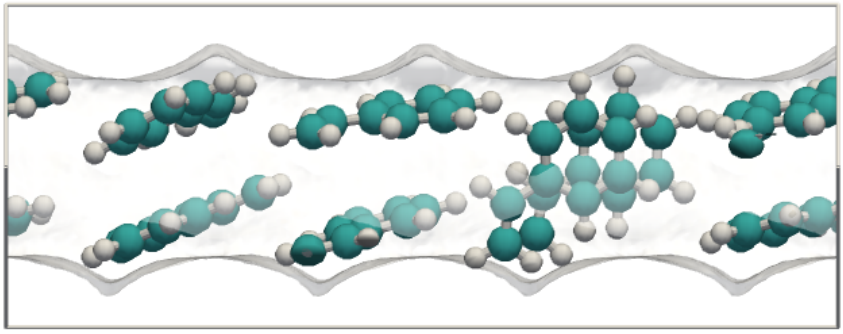

(a) *Styrene*

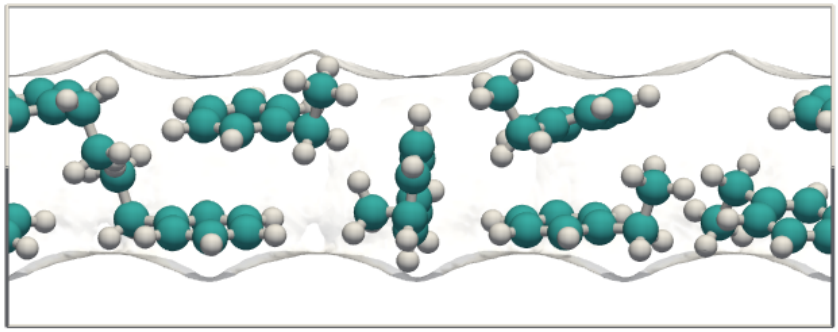

(b) *Ethylbenzene*

Figure S16: *Snapshots of styrene (top) and ethylbenzene (bottom) in MIL-47 at 1e9 Pa and 433K. Both, ethylbenzene and styrene molecules have commensurate stacking. However the "length" of the packing of styrene in the channels is smaller. This allows styrene to obtain a higher saturation capacity than ethylbenzene. MIL-47 is a styrene selective structure. Color code: carbon (cyan), hydrogen (white).*

2.6.2 Langmuir-Freundlich parameters

	site A			site B		
	$q_{i,A,\text{sat}}$ [mol kg^{-1}]	$b_{i,A}$ [Pa$^{-\nu_{i,A}}$]	$\nu_{i,A}$ [-]	$q_{i,B,\text{sat}}$ [mol kg^{-1}]	$b_{i,B}$ [Pa$^{-\nu_{i,B}}$]	$\nu_{i,B}$ [-]
styrene	1.4	4.11×10^{-4}	0.67	2.9	1.89×10^{-3}	1.1
ethylbenzene	1.2	3.45×10^{-3}	0.44	2.3	3.73×10^{-3}	1.1

Table S6: *Dual-site Langmuir-Freundlich parameters for pure component xylene isomers at 433 K in MIL-47.*

2.6.3 Adsorption isotherms

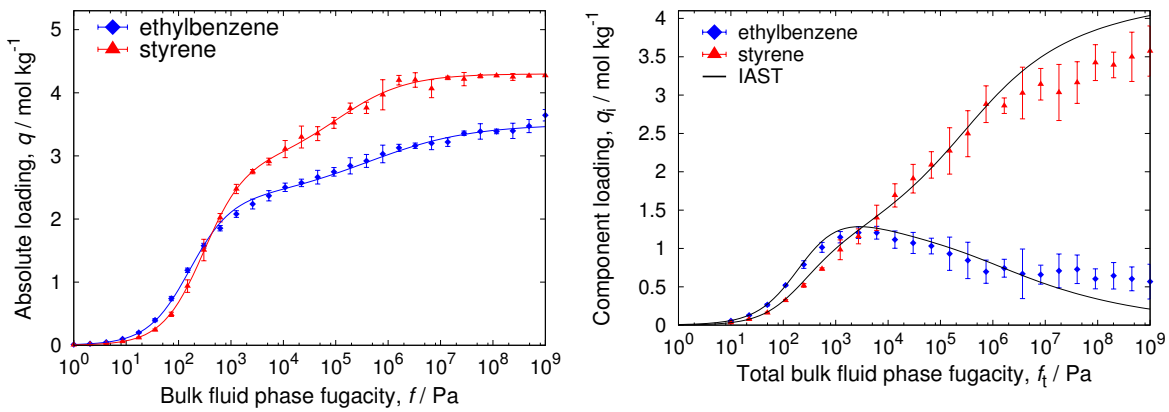

(a) **(b)**

Figure S17: *Simulated isotherms of styrene and ethylbenzene in MIL-47 at 433K. (a) Pure component isotherms (lines are dual-site Langmuir-Freundlich fits of the pure components, points are the pure component isotherms from CB/CFCMC simulations) and mixture component isotherms for an equimolar mixture. The IAST results are in good agreement with the mixture isotherms*

2.6.4 Breakthrough simulations

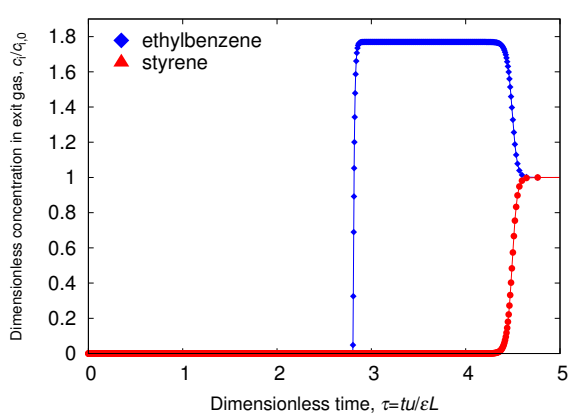

Figure S18: *Simulated step-type breakthrough of styrene and ethylbenzene in MIL-47 at 433K and 1e6 Pa total fugacity. Video animations of the breakthrough behavior as a function of time are provided as Supplementary information.*

2.7 MAF-X8: commensurate stacking

2.7.1 Snapshots

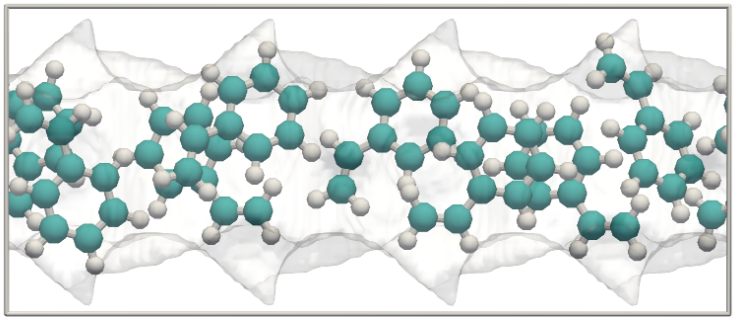

(a) *XY-view styrene*

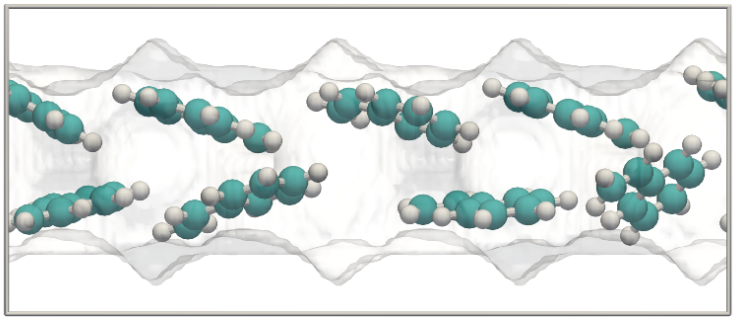

(b) *YZ-view styrene*

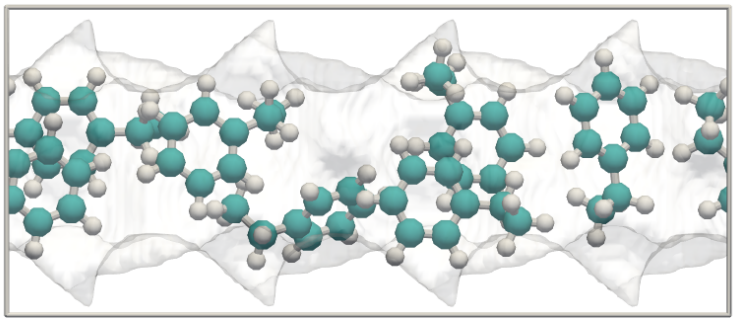

(c) *XY-view ethylbenzene*

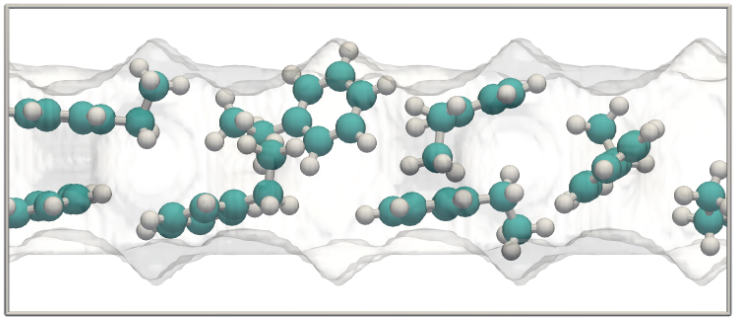

(d) *YZ-view ethylbenzene*

Figure S19: *Snapshots of styrene (top) and ethylbenzene (bottom) in MAF-X8 at 1e9 Pa and 433K. Both styrene and ethylbenzene have commensurate stacking. Color code: carbon (cyan), hydrogen (white).*

2.7.2 Adsorption isotherms

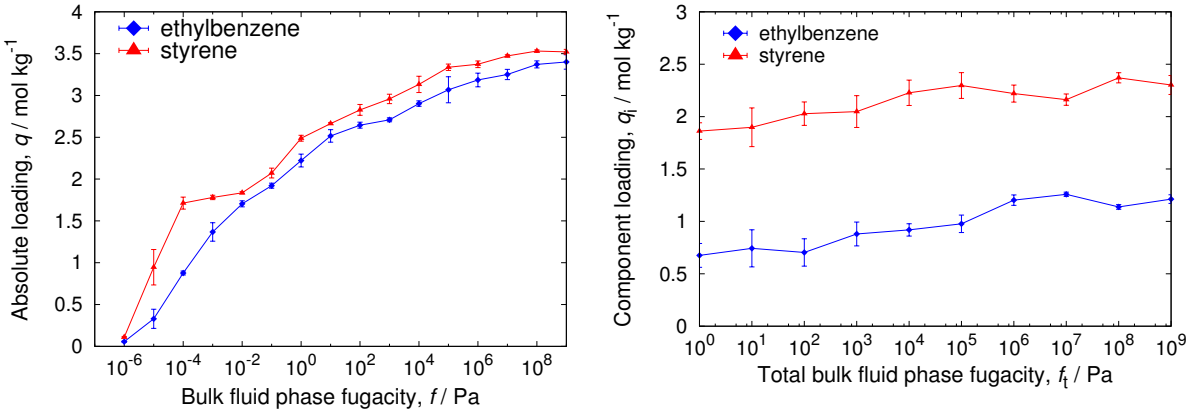

(a) **(b)**

Figure S20: *Simulated isotherms of styrene and ethylbenzene in MAF-X8 at 433K. (a) Pure component isotherms from CB/CFCMC simulations (b) mixture component isotherms for an equimolar mixture.*

2.8 MOF-CJ3: combination of effects

2.8.1 Snapshots

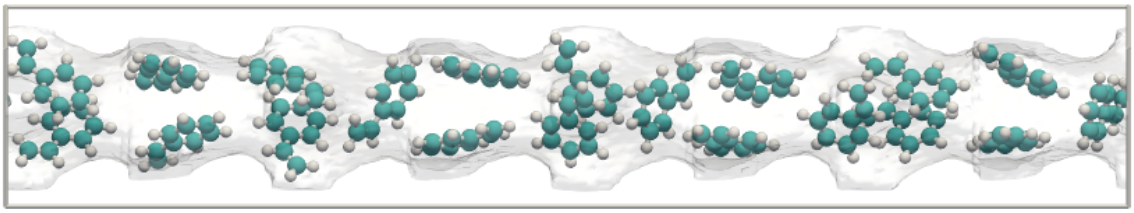

(a) *XZ-view styrene*

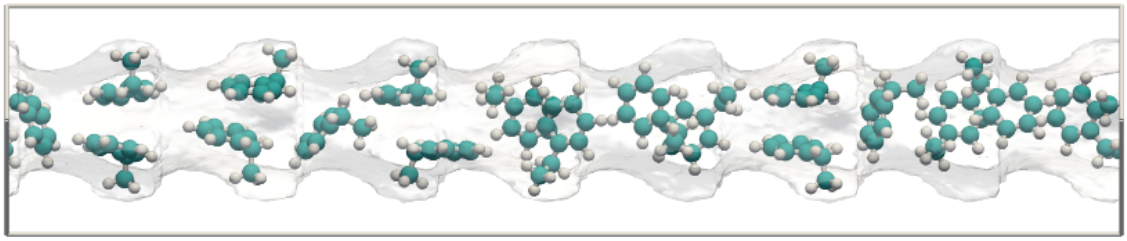

(b) *XZ-view ethylbenzene*

Figure S21: *Snapshots of styrene (top) and ethylbenzene (bottom) in MOF-CJ3 at 1e9 Pa and 433K. Color code: carbon (cyan), hydrogen (white).*

2.8.2 Langmuir-Freundlich parameters

2.8.3 Adsorption isotherms

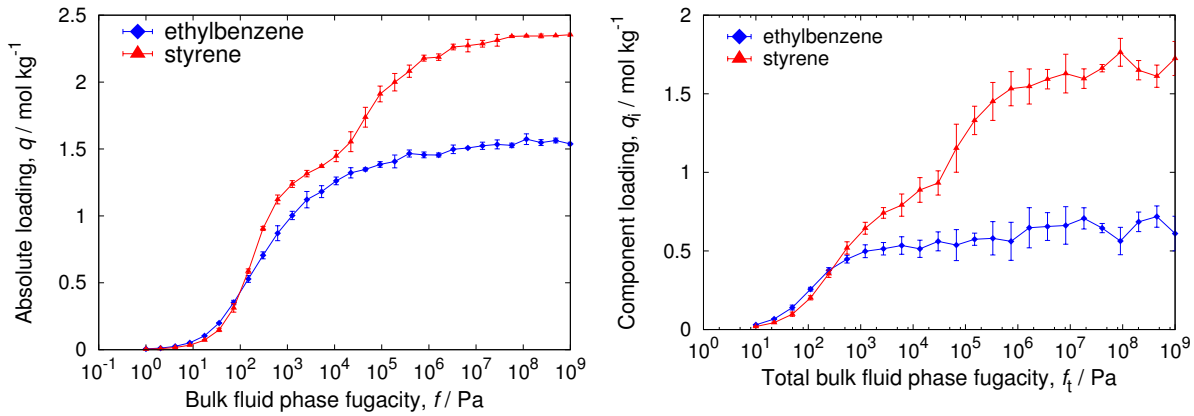

(a) **(b)**

Figure S22: *Simulated isotherms of styrene and ethylbenzene in MOF-CJ3 at 433K. (a) Pure component isotherms (b) mixture component isotherms for an equimolar mixture.*

2.8.4 Breakthrough simulations

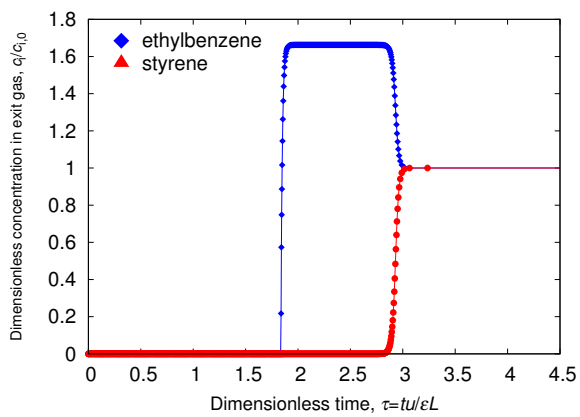

Figure S23: *Simulated step-type breakthrough of styrene and ethylbenzene in MOF-CJ3 at 433K and 1e6 Pa total fugacity. Video animations of the breakthrough behavior as a function of time are provided as Supplementary information.*

2.9 Snapshots MRE

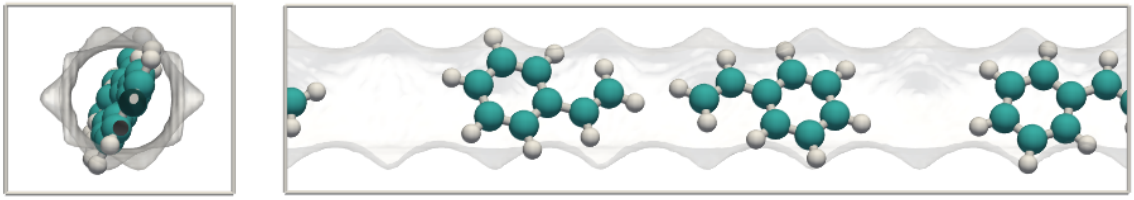

(a) *styrene*

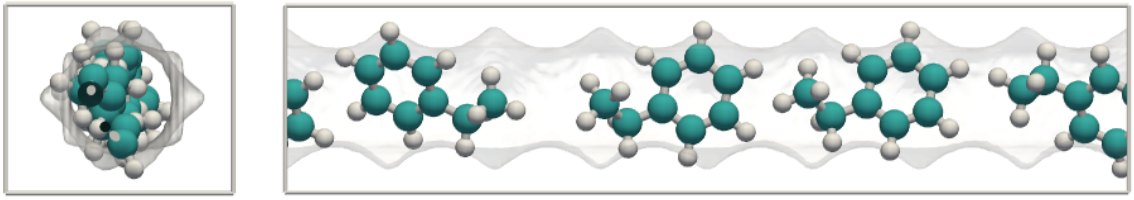

(b) *ethylbenzene*

Figure S24: *Snapshots of styrene and ethylbenzene in MRE zeolite at 433K and 1e9 Pa. The channel dimensions are only large enough for molecules to be adsorb parallel to the channel axis. Because styrene and ethylbenzene main difference is their height (non-planarity of ethyl group) and not the molecule's lengths, their saturation capacity will be very similar. Color code: carbon (cyan), hydrogen (white).*

2.10 Snapshots MTW

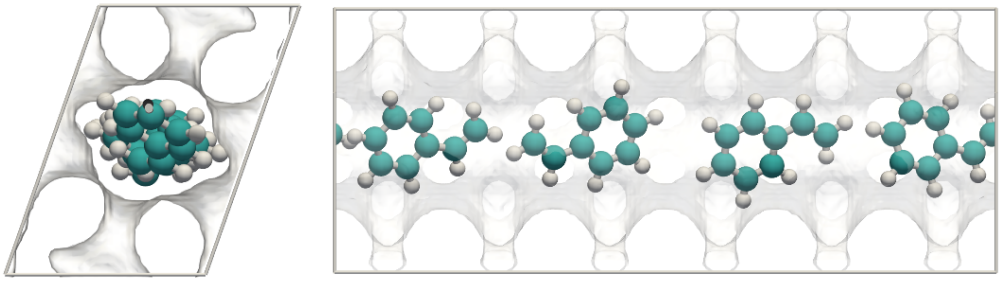

(a) *styrene*

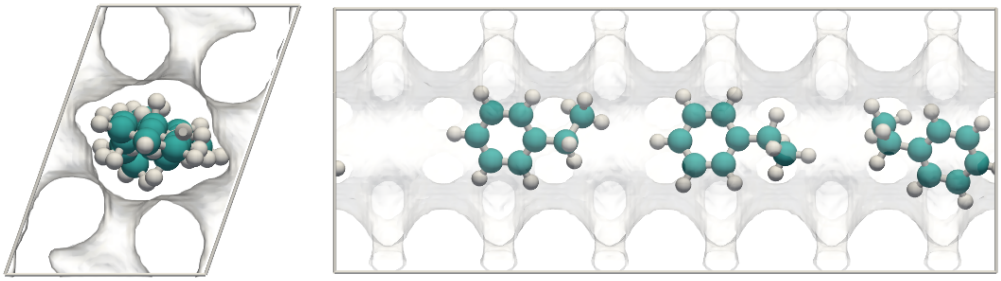

(b) *ethylbenzene*

Figure S25: *Snapshots of styrene and ethylbenzene in MTW zeolite at 433K and 1e9 Pa. As in MRE, because both molecules have a very similar length and they can only adsorb parallel to the channel axis, no mayor difference will be observed in the saturation capacity of these molecules. Color code: carbon (cyan), hydrogen (white).*

2.10.1 Mixture isotherms IRMOF-1, JUC-77, MIL-125, CoBDP

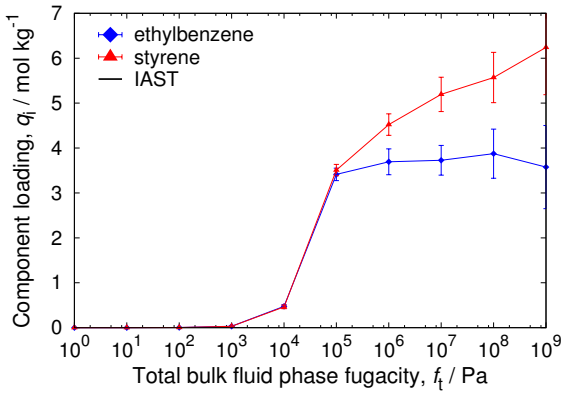

(a)

Figure S26: *Simulated mixture component isotherms in IRMOF-1at 433K.*

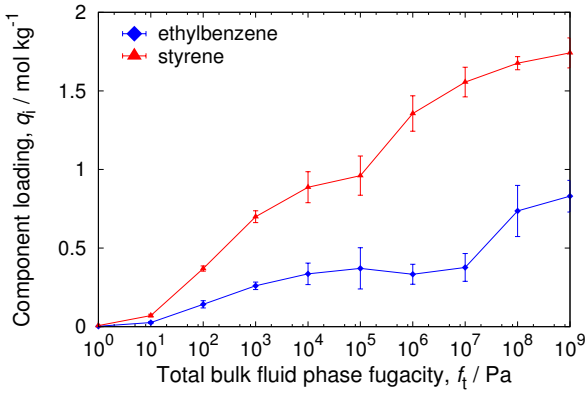

Figure S27: *Simulated mixture component isotherms in JUC-77 at 433K.*

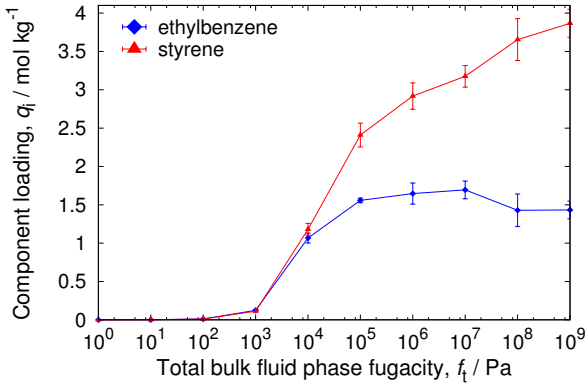

Figure S28: *Simulated mixture component isotherms in MIL-125 at 433K.*

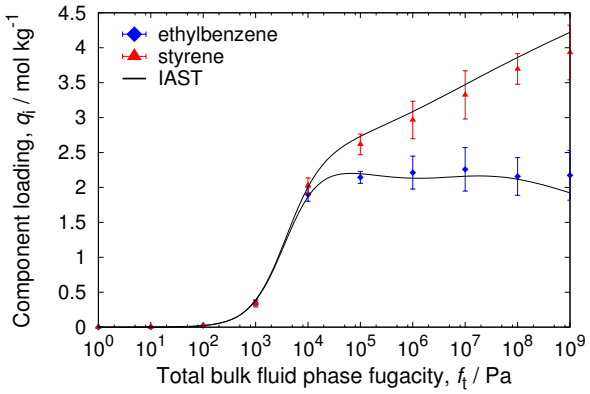

Figure S29: *Simulated mixture component isotherms in CoBDP at 433K.*

3

Selectivity in styrene/ethylbenzene equimolar mixture

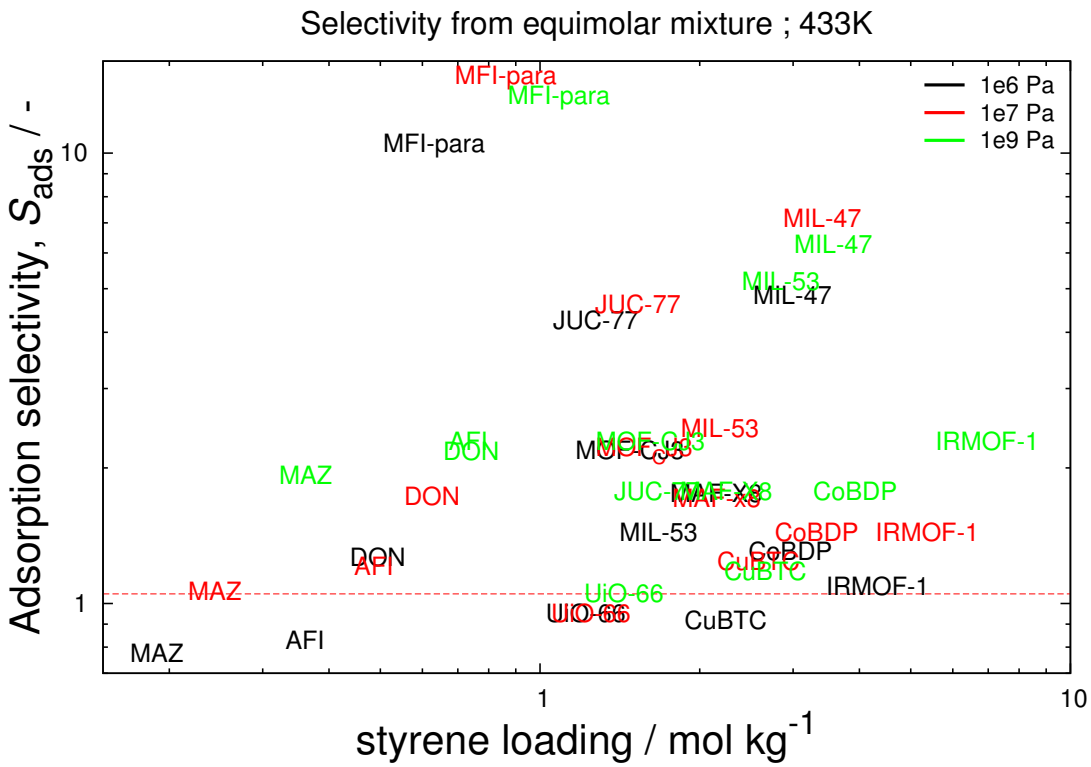

Figure S30: *Selectivity (q_{st}/q_{eb}) in an equimolar mixture at 3 different fugacities. The dashed red line corresponds to the liquid phase ratio. For all the cases styrene loading increases with the fugacity (shift to the right of the plot). The selectivity also increases in most of the cases with the fugacity (shift upwards) except for MFI-para, JUC-77, MIL-47 and Cu-BTC.*

3.1 Zeolites: small pore volumes

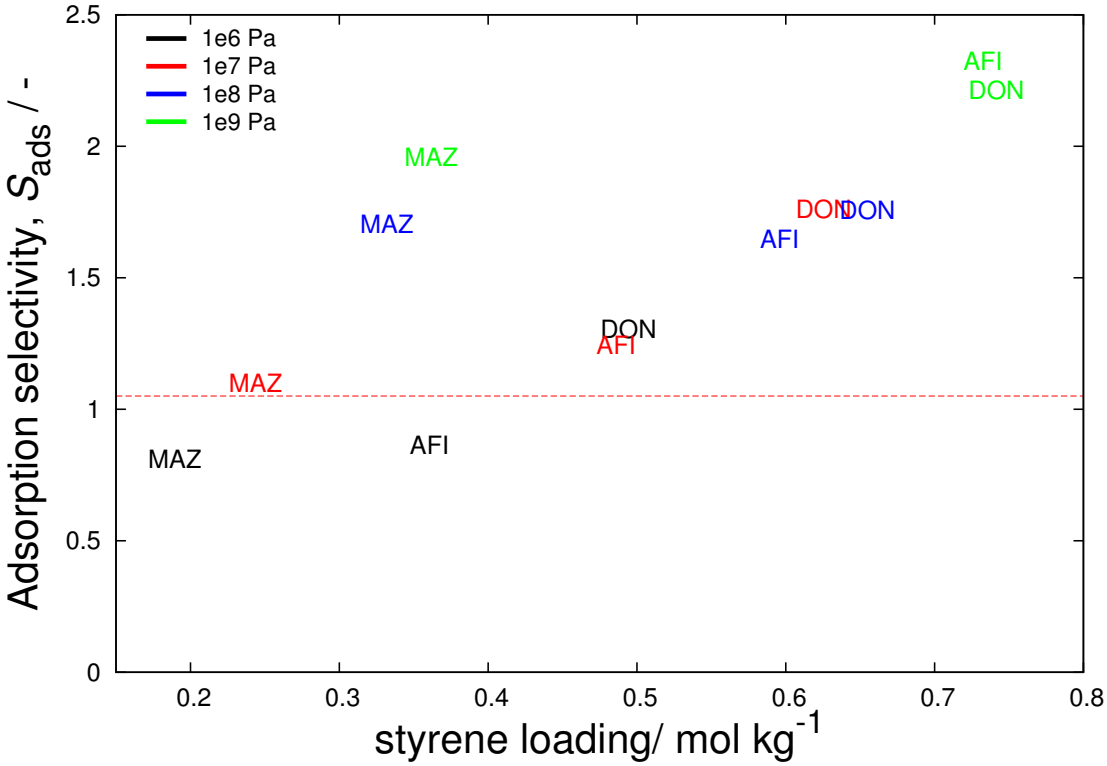

Figure S31: *Zoom in of Figure S30 in the zeolites region (low loading). The dashed red line corresponds to the liquid phase ratio.*

3.2 Interesting cases for the separation

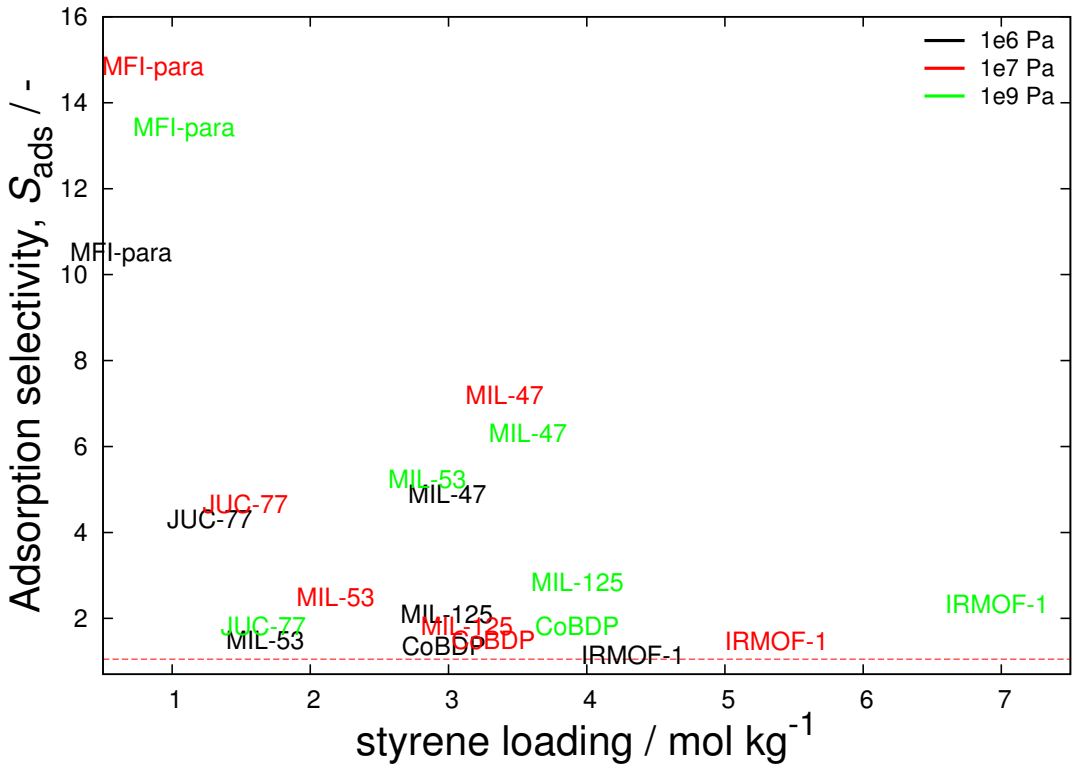

Figure S32: *Selectivity as a function of styrene loading for different fugacities in zeolites and metal-organic frameworks with interesting properties for the separation of styrene and ethylbenzene mixtures. The dashed red line corresponds to the liquid phase ratio.*

4

Screening of Potential Zeolite Adsorbents

4.1 AFI

unit cell size	$a = b = 13.827[\AA]$, $c = 8.58[\AA]$
unit cell angles	$\alpha = \beta = 90[°]$, $\gamma = 120[°]$
unit cells	$3 \times 3 \times 5$
framework density	1685.573 [kg/m^3]
description	AFI-type zeolite
crystallographic data	ref. [10]
void fraction	0.283131 [-]
accessible pore volume	0.1679 [cm^3/g]
nitrogen surface area	548 [m^2/g],924 [m^2/cm^3]
optimization	-
charges	REPEAT with PES from VASP

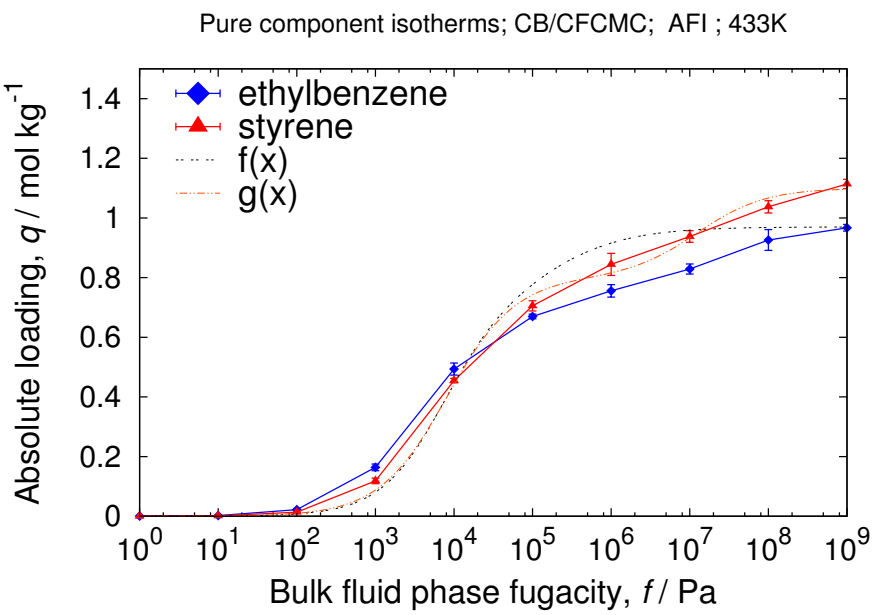

4.2 BEA

unit cell size	$a = b = 12.632[\AA]$, $c = 26.186[\AA]$
unit cell angles	$\alpha = \beta = \gamma = 90[°]$
unit cells	$2 \times 2 \times 1$
framework density	1528.187 [kg/m^3]
description	BEA zeolite
crystallographic data	ref. [11]
void fraction	0.421281 [-]
accessible pore volume	0.2756 [cm^3/g]
nitrogen surface area	994 [m^2/g], 1519 [m^2/cm^3]
optimization	-
charges	REPEAT with PES from VASP

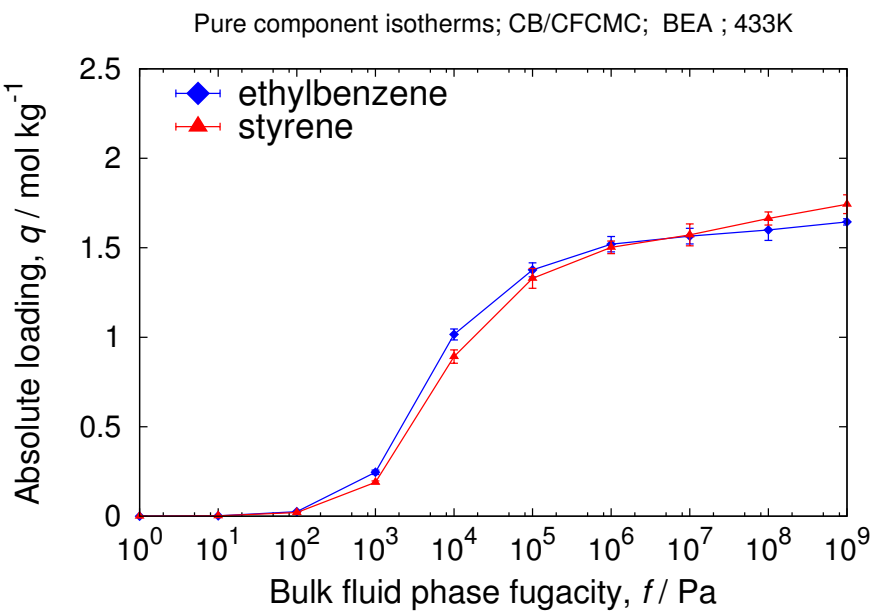

4.3 DON

unit cell size	$a = 18.89[\AA]$, $b = 23.365[\AA]$, $c = 8.46[\AA]$
unit cell angles	$\alpha = \beta = \gamma = 90[°]$
unit cells	$2 \times 2 \times 4$
framework density	1708.2843 [kg/m^3]
description	DON zeolite
crystallographic data	ref. [12]
void fraction	0.287907 [-]
accessible pore volume	0.16853 [cm^3/g]
nitrogen surface area	525 [m^2/g], 897 [m^2/cm^3]
optimization	-
charges	REPEAT with PES from VASP

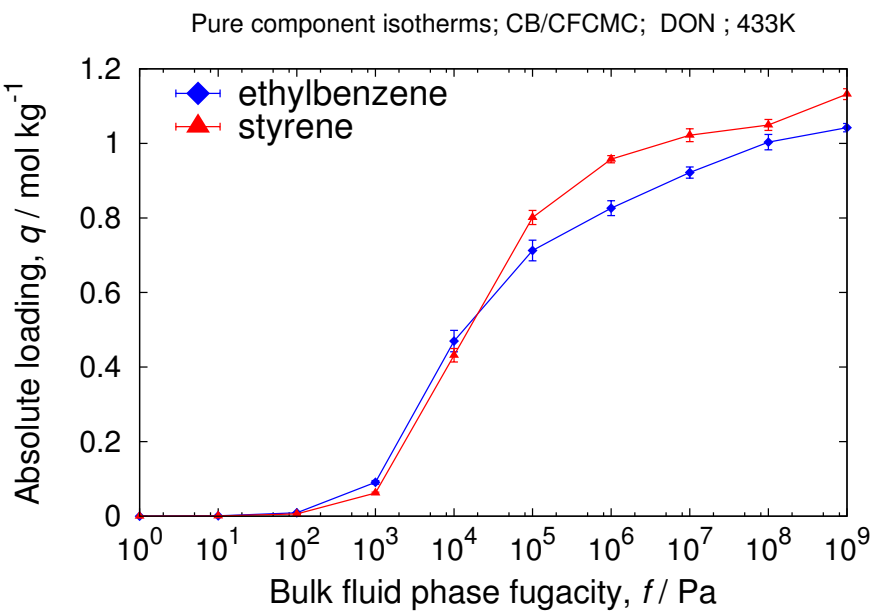

4.4 EMT

unit cell size	$a = b = 17.215[\AA]$, $c = 28.082[\AA]$
unit cell angles	$\alpha = \beta = 90[°]$, $\gamma = 120[°]$
unit cells	$2 \times 2 \times 1$
framework density	1328.9498 [kg/m^3]
description	EMT zeolite
crystallographic data	ref. [13]
void fraction	0.492004 [-]
accessible pore volume	0.3702 [cm^3/g]
nitrogen surface area	1136 [m^2/g], 1510 [m^2/cm^3]
optimization	-
charges	REPEAT with PES from VASP

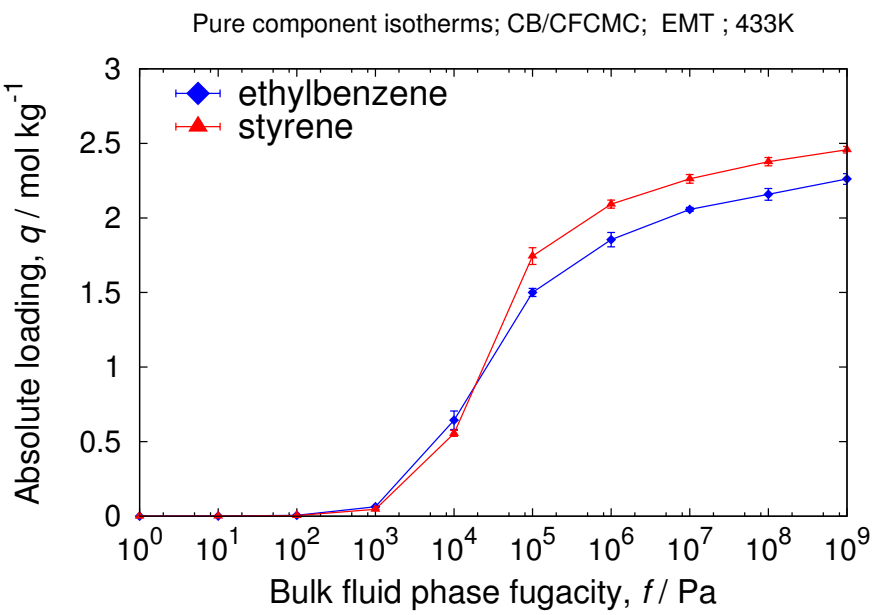

4.5 MAZ

unit cell size	$a = b = 18.1020[\AA]$, $c = 7.6180[\AA]$
unit cell angles	$\alpha = \beta = 90[°]$, $\gamma = 120[°]$
unit cells	$2 \times 2 \times 4$
framework density	1661.4522 [kg/m^3]
description	MAZ zeolite
crystallographic data	ref. [14]
void fraction	0.279375 [-]
accessible pore volume	0.1681 [cm^3/g]
nitrogen surface area	534 [m^2/g], 888 [m^2/cm^3]
optimization	-
charges	REPEAT with PES from VASP

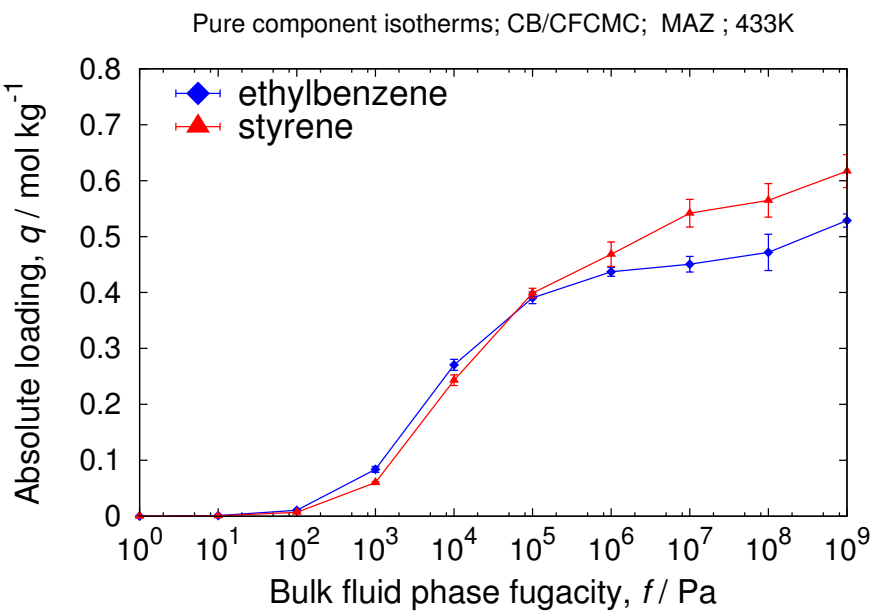

4.6 MFI(Olson)

unit cell size	$a = 20.07[\AA]$, $b = 19.92[\AA]$,$c = 13.42[\AA]$
unit cell angles	$\alpha = \beta = \gamma = 90[°]$
unit cells	$2 \times 2 \times 2$
framework density	1785.2214 [kg/m^3]
description	MFI-Olson zeolite
crystallographic data	ref. [15]
void fraction	0.2988 [-]
accessible pore volume	0.16738 [cm^3/g]
nitrogen surface area	599 [m^2/g], 1069 [m^2/cm^3]
optimization	-
charges	REPEAT with PES from VASP

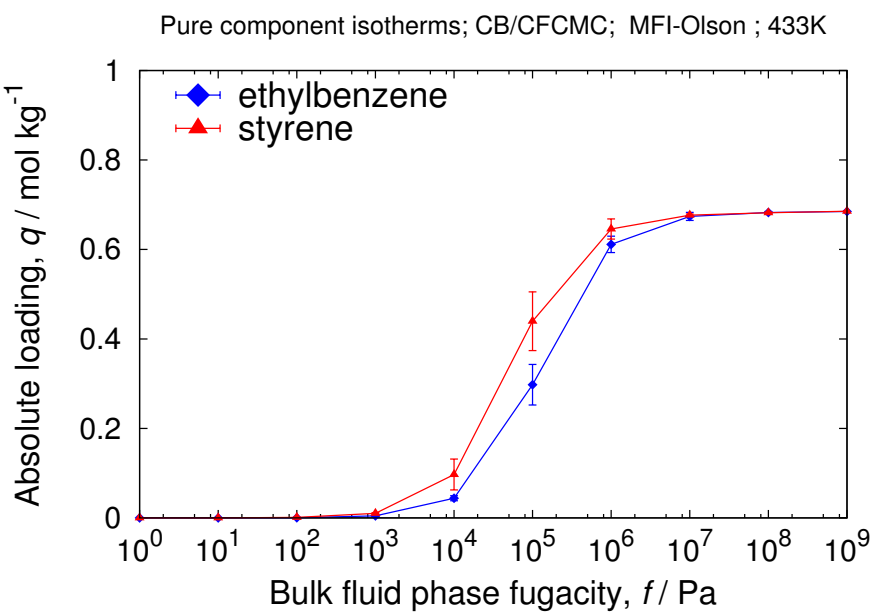

4.7 MFI(Van Koningsveld)

unit cell size	$a = 20.022, b = 19.899, c = 13.383[\AA]$
unit cell angles	$\alpha = \beta = \gamma = 90[°]$
unit cells	$2 \times 2 \times 2$
framework density	1796.3424 [kg/m^3]
description	MFI zeolite
crystallographic data	ref. [16]
void fraction	0.294147 [-]
accessible pore volume	0.1637 [cm^3/g]
nitrogen surface area	584 [m^2/g], 1050 [m^2/cm^3]
optimization	-
charges	REPEAT with PES from VASP

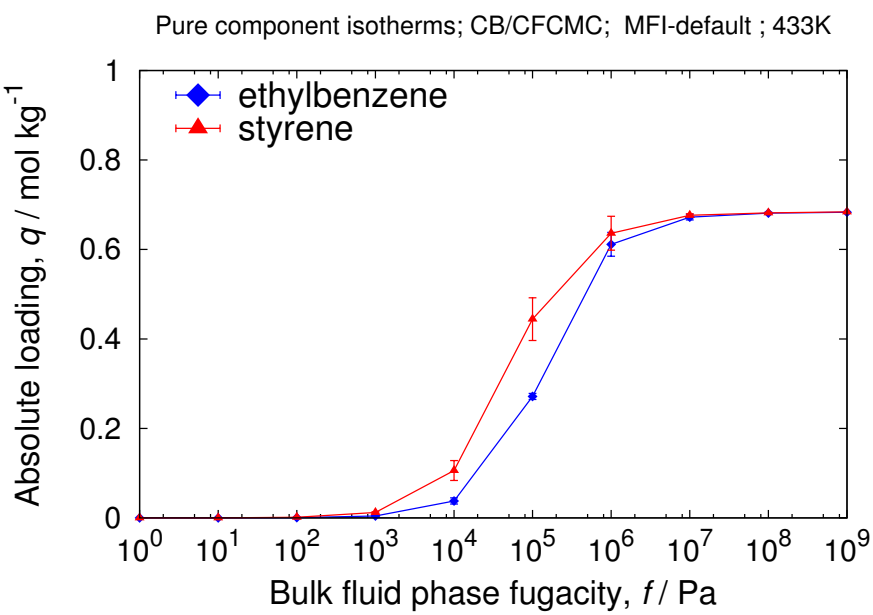

4.8 MFI-mono

unit cell size	$a = 20.1087[\AA]$,$b = 19.879[\AA]$ [Å] $c = 8.58[\AA]$
unit cell angles	$\alpha = 90.67[°]$, $\beta = \gamma = 90[°]$
unit cells	$2 \times 2 \times 2$
framework density	1792.54[kg/m^3]
description	MFI-mono zeolite
crystallographic data	ref. [17]
void fraction	0.2860
accessible pore volume	0.1595
nitrogen surface area	663 [m^2/g],1188 [m^2/cm^3]
optimization	-
charges	REPEAT with PES from VASP

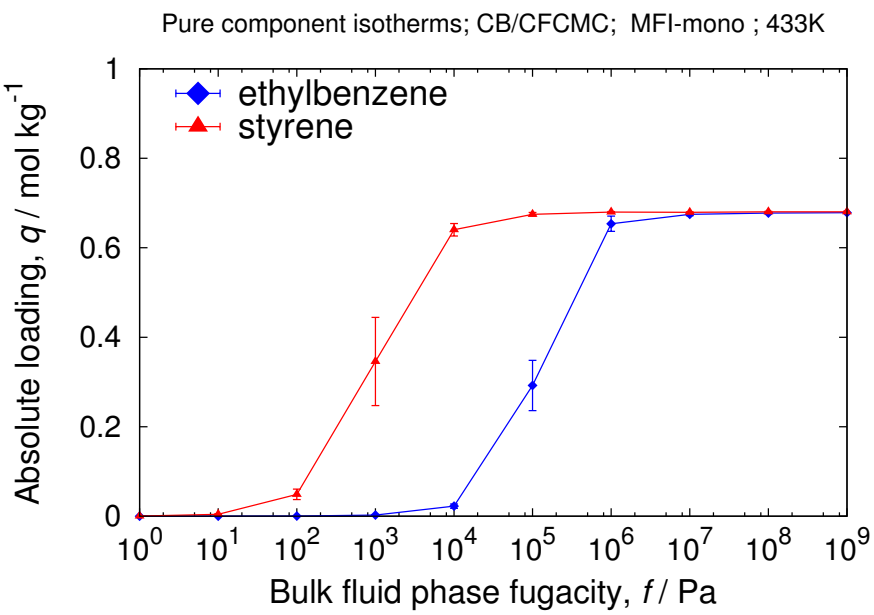

4.9 MFI-para

unit cell size	$a = 20.121[\AA]$, $b = 19.82[\AA]$,$c = 13.43[\AA]$
unit cell angles	$\alpha = \beta = \gamma = 90[°]$
unit cells	$2 \times 2 \times 2$
framework density	1787.2835 [kg/m^3]
description	MFI-para zeolite
crystallographic data	ref. [18]
void fraction	0.278585 [-]
accessible pore volume	0.15587 [cm^3/g]
nitrogen surface area	602 [m^2/g], 1076 [m^2/cm^3]
optimization	-
charges	REPEAT with PES from VASP

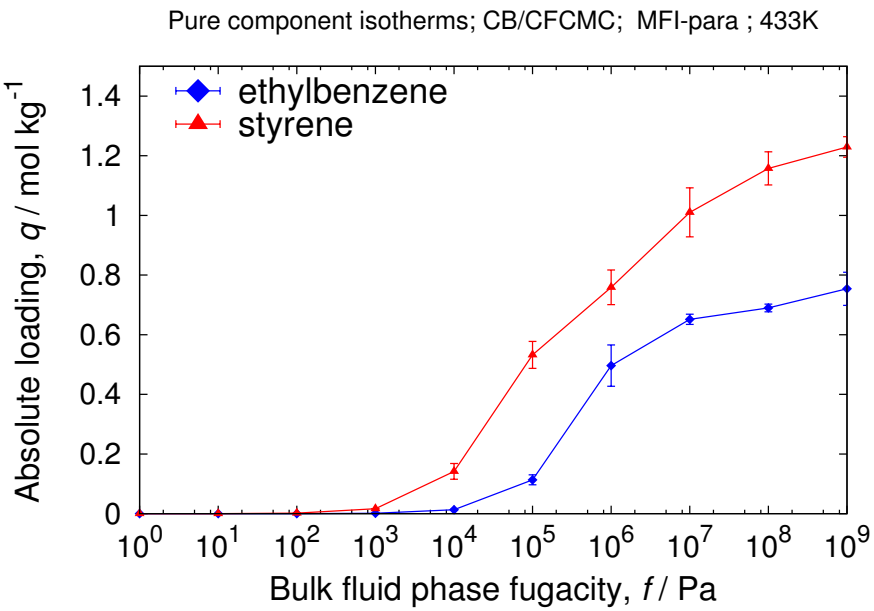

4.10 MOR

unit cell size	$a = 18.256, b = 20.534, c = 7.542[\check{A}]$
unit cell angles	$\alpha = \beta = \gamma = 90[°]$
unit cells	$2 \times 2 \times 4$
framework density	1693.8915 [kg/m^3]
description	MOR zeolite
crystallographic data	ref. [19]
void fraction	0.267676 [-]
accessible pore volume	0.15802 [cm^3/g]
nitrogen surface area	994 [m^2/g], 1519 [m^2/cm^3]
optimization	-
charges	REPEAT with PES from VASP

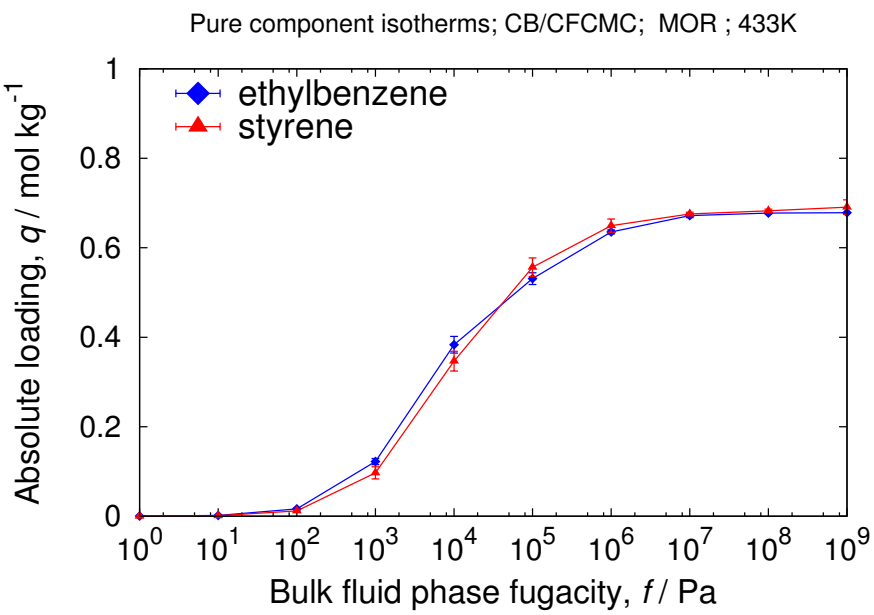

4.11 MRE

unit cell size	$a = 8.257[\AA]$, $b = 14.562[\AA]$, $c = 20.314[\AA]$
unit cell angles	$\alpha = \beta = \gamma = 90[°]$
unit cells	$4 \times 2 \times 2$
framework density	1960.706 [kg/m^3]
description	MRE-type, ZSM-48
crystallographic data	ref. [20, 21]
void fraction	0.175396 [-]
accessible pore volume	0.0894 [cm^3/g]
nitrogen surface area	573 [m^2/g], 292 [m^2/cm^3]
optimization	-
charges	REPEAT with PES from VASP

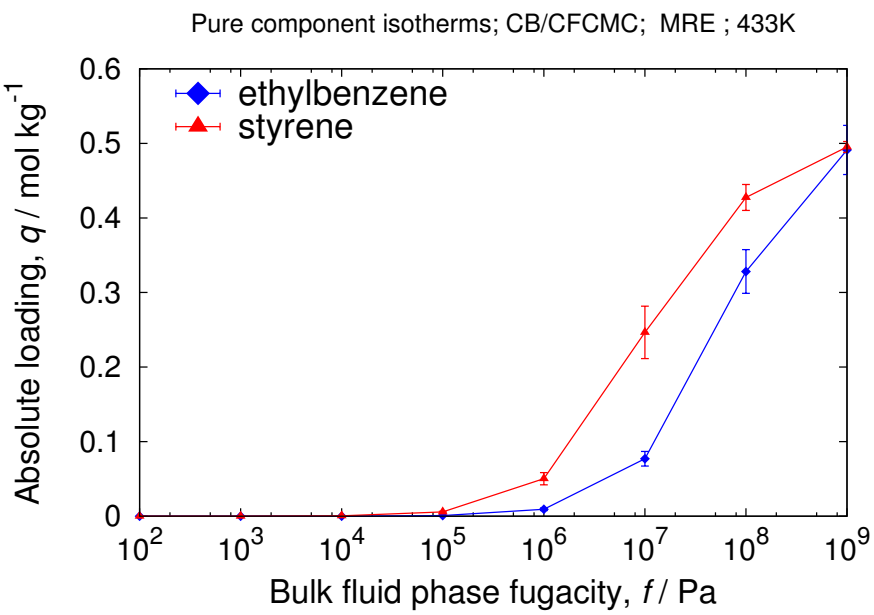

4.12 MTW

unit cell size	$a = 25.552[\AA]$, $b = 5.256[\AA]$, $c = 12.117[\AA]$
unit cell angles	$\alpha = 90[°]$, $\beta = 109.312[°]$, $\gamma = 90[°]$
unit cells	$1 \times 6 \times 3$
framework density	1819.048 [kg/m^3]
description	MTW-type zeolite
crystallographic data	ref. [22]
void fraction	0.211619 [-]
accessible pore volume	0.11633 [cm^3/g]
nitrogen surface area	818 [m^2/g], 450 [m^2/cm^3]
optimization	-
charges	REPEAT with PES from VASP

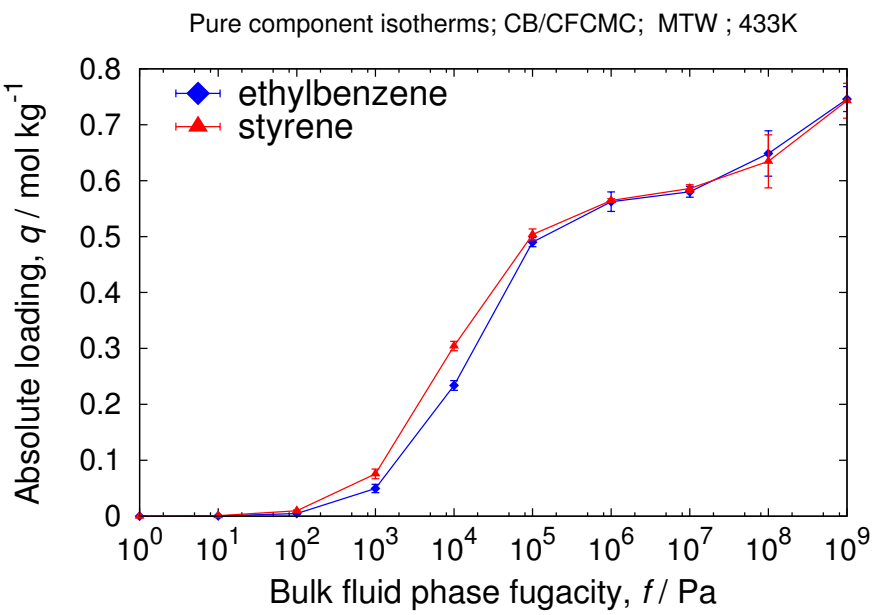

4.13 LTL

unit cell size	$a = b = 18.126[\AA]$,$c = 7.56[\AA]$
unit cell angles	$\alpha = \beta = 90[°]$,$\gamma = 120[°]$
unit cells	$2 \times 2 \times 4$
framework density	1668.2235 [kg/m^3]
description	LTL zeolite
crystallographic data	ref. [23]
void fraction	0.5193 [-]
accessible pore volume	0.3115 [cm^3/g]
nitrogen surface area	550 [m^2/g], 918 [m^2/cm^3]
optimization	-
charges	REPEAT with PES from VASP

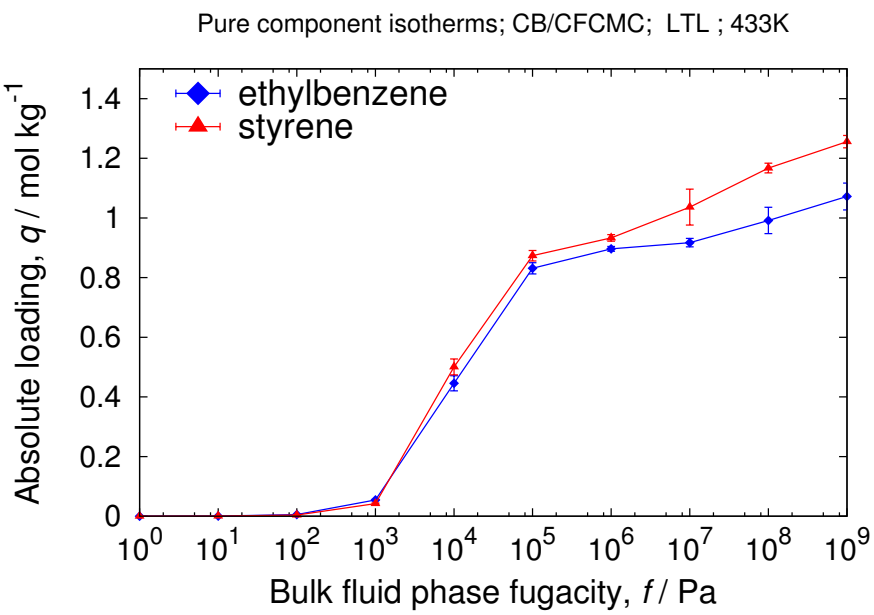

5

Screening of Potential MOF Adsorbents

5.1 CoBDP

unit cell size	$a = 13.253[\AA]$, $b = 13.253[\AA]$, $c = 13.995[\AA]$
unit cell angles	$\alpha = \beta = \gamma = 90[°]$
unit cells	$2 \times 2 \times 3$
framework density	721.88 [kg/m^3]
description	Co(BDP)
crystallographic data	ref. [24]
void fraction	0.6535 [-]
accessible pore volume	0.9053 [cm^3/g]
nitrogen surface area	2244 [m^2/g], 1620 [m^2/cm^3]
optimization	VASP fixed cell, PBE, precision=high
charges	REPEAT with PES from VASP

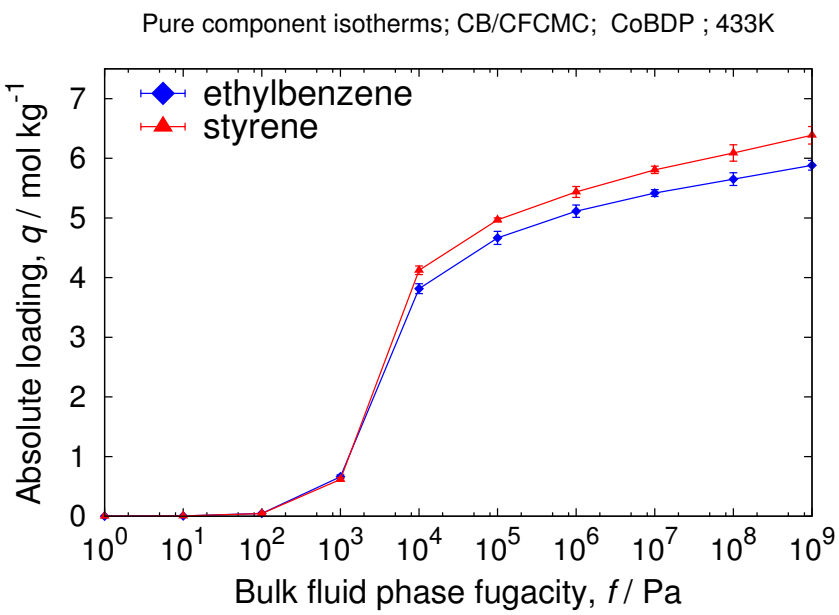

5.2 CoDOBDC

unit cell size	$a = 25.885[\AA]$, $b = 25.885[\AA]$, $c = 6.8058[\AA]$
unit cell angles	$\alpha = \beta = 90, \gamma = 120[°]$
unit cells	$2 \times 2 \times 4$
framework density	1180.56 [kg/m^3]
description	Co(DOBDC)
crystallographic data	ref. [25]
void fraction	0.706 [-]
accessible pore volume	0.59811 [cm^3/g]
nitrogen surface area	1338[m^2/g], 1580[m^2/cm^3]
optimization	-
charges	REPEAT with PES from VASP

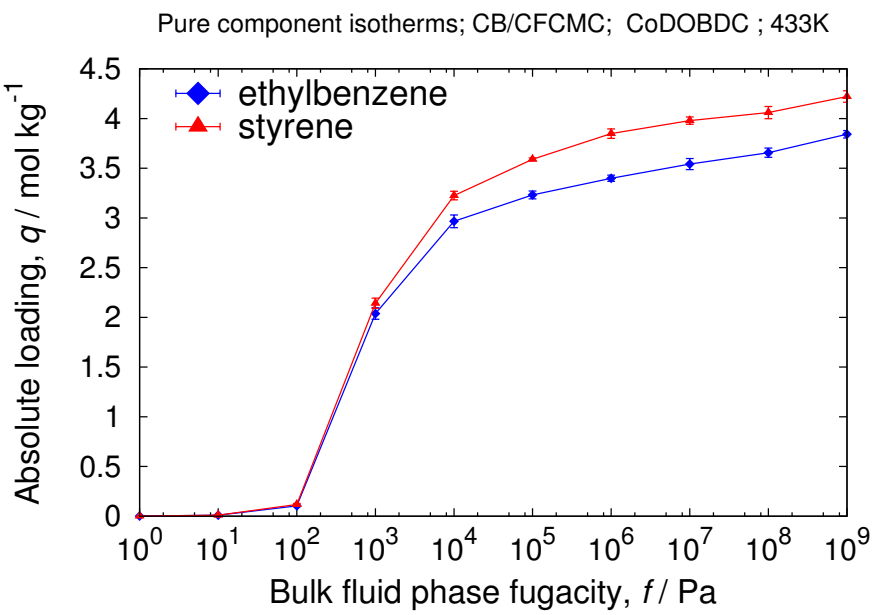

5.3 Cu-BTC

unit cell size	$a = b = c = 18.6273[\AA]$
unit cell angles	$\alpha = \beta == 60[°]$
unit cells	$2 \times 2 \times 2$
framework density	1685.573 [kg/m^3]
description	Cu-BTC
crystallographic data	ref. [26]
void fraction	0.283131 [-]
accessible pore volume	0.1679 [cm^3/g]
nitrogen surface area	548 [m^2/g],924 [m^2/cm^3]
optimization	-
charges	REPEAT with PES from VASP

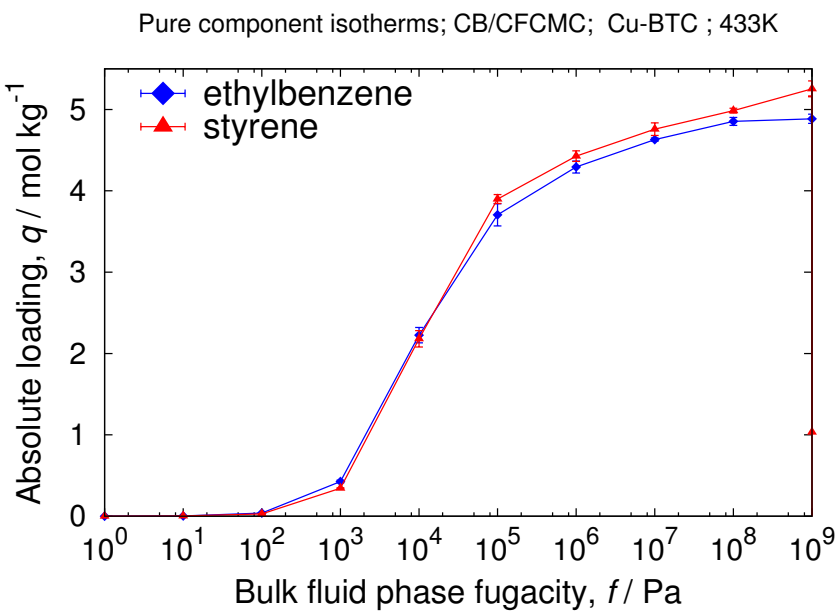

5.4 IRMOF-1

unit cell size	$a = b = c = 18.2660[\AA]$
unit cell angles	$\alpha = \beta = \gamma = 60[°]$
unit cells	$2 \times 2 \times 2$
framework density	593.394 [kg/m^3]
description	IRMOF-1
crystallographic data	ref. [27]
void fraction	0.8038[-]
accessible pore volume	0.9271[cm^3/g]
nitrogen surface area	3592 [m^2/g], 2131 [m^2/cm^3]
optimization	-
charges	REPEAT with PES from VASP

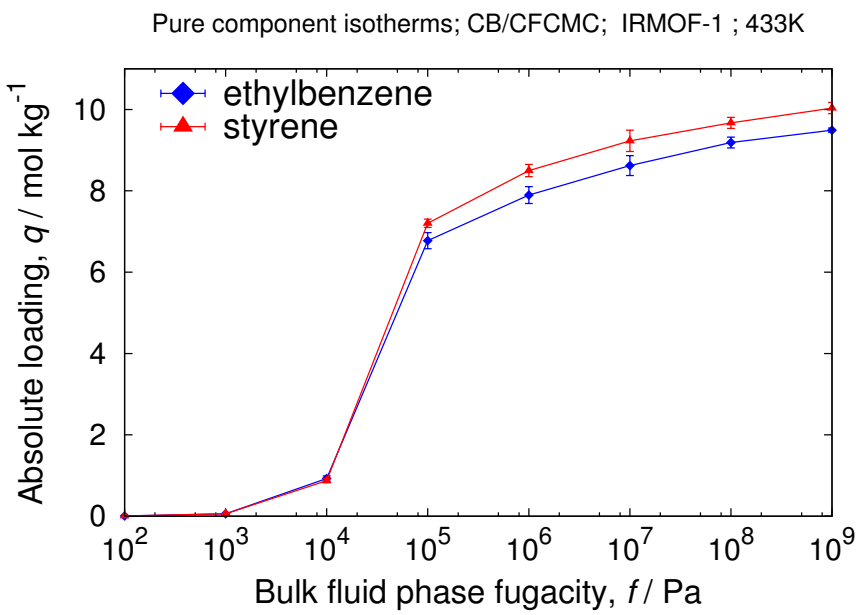

5.5 JUC-77

unit cell size	$a = 13.985[\AA]$, $b = 25.205[\AA]$, $c = 24.996[\AA]$
unit cell angles	$\alpha = 32.34, \beta = 74.65, \gamma = 73.003[°]$
unit cells	$2 \times 2 \times 2$
framework density	1144.03 [kg/m^3]
description	JUC-77
crystallographic data	ref. [28]
void fraction	0.4783 [-]
accessible pore volume	0.4181 [cm^3/g]
nitrogen surface area	1098 [m^2/g], 1256 [m^2/cm^3]
optimization	VASP fixed cell, PBE, precision=high
charges	REPEAT with PES from VASP

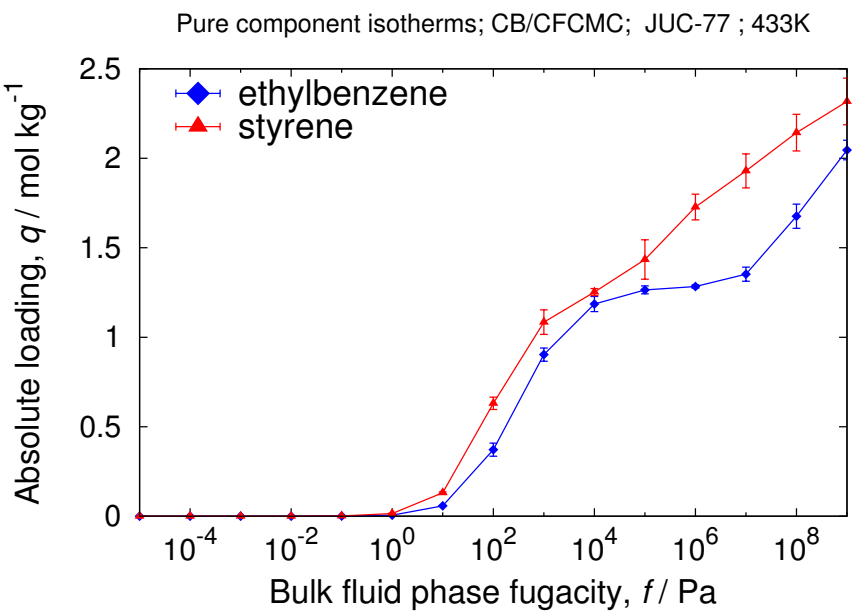

5.6 MAF-X8

unit cell size	$a = 13.9249[\AA]$, $b = 23.653[\AA]$, $c = 23.637[\AA]$
unit cell angles	$\alpha = \beta = \gamma = 90[°]$
unit cells	$2 \times 2 \times 2$
framework density	954.2915 [kg/m^3]
description	MAF-x8
crystallographic data	ref. [29]
void fraction	0.4947[-]
accessible pore volume	0.5184 [cm^3/g]
nitrogen surface area	1465 [m^2/g], 1397 [m^2/cm^3]
optimization	-
charges	REPEAT with PES from VASP

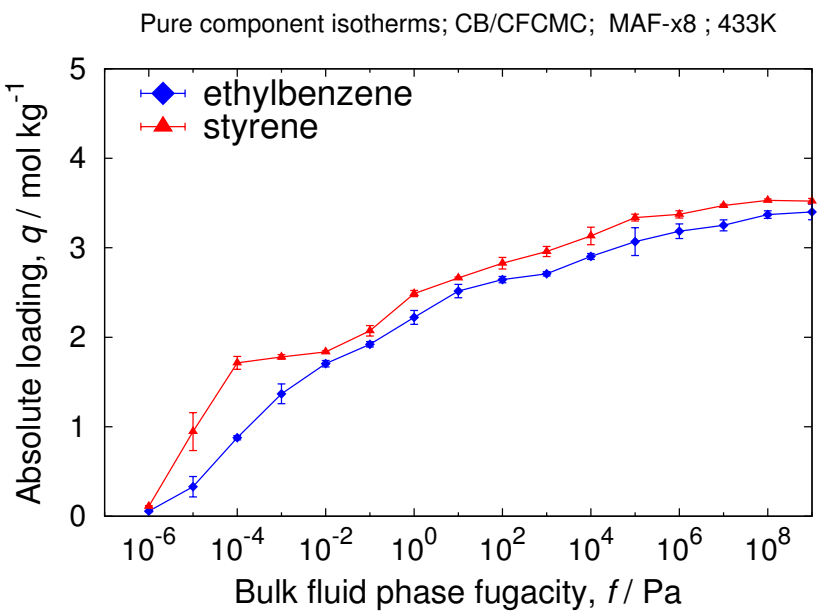

5.7 MIL-47

unit cell size	$a = 6.8179[\AA]$, $b = 16.143[\AA]$, $c = 13.939[\AA]$
unit cell angles	$\alpha = \beta = \gamma = 90[°]$
unit cells	$4 \times 2 \times 2$
framework density	1000.36 [kg/m^3]
description	MIL-47
crystallographic data	ref. [30]
void fraction	0.6088 [-]
accessible pore volume	0.6086 [cm^3/g]
nitrogen surface area	1655 [m^2/g], 1656 [m^2/cm^3]
optimization	-
charges	REPEAT with PES from VASP

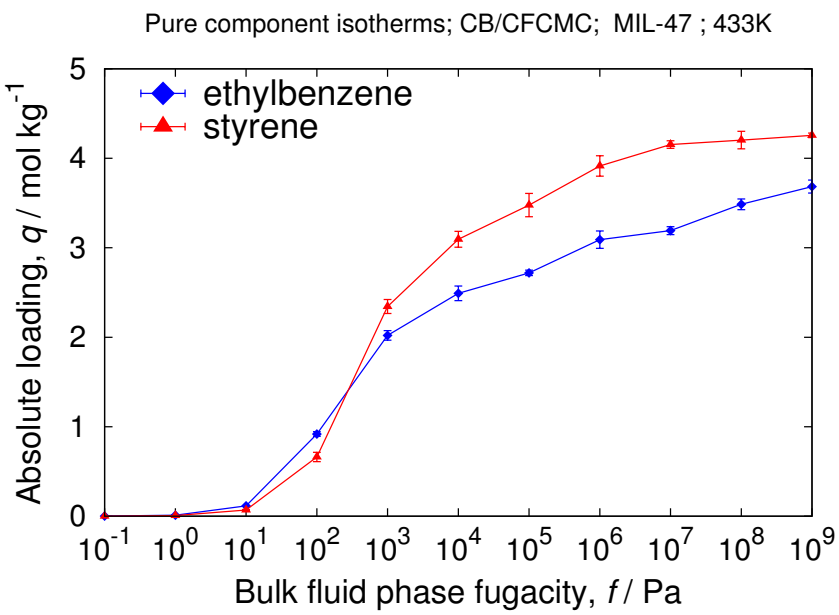

5.8 MIL-53

unit cell size	$a = 16.73300[\AA]$, $b = 13.038[\AA]$, $c = 6.8120[\AA]$
unit cell angles	$\alpha = \beta = \gamma = 90[^\circ]$
unit cells	$2 \times 2 \times 4$
framework density	$1041.90[kg/m^3]$
description	MIL-53
crystallographic data	ref. [31]
void fraction	0.5501[-]
accessible pore volume	$0.5279[cm^3/g]$
nitrogen surface area	$1435[m^2/g]$,$1495[m^2/cm^3]$
optimization	-
charges	REPEAT with PES from VASP

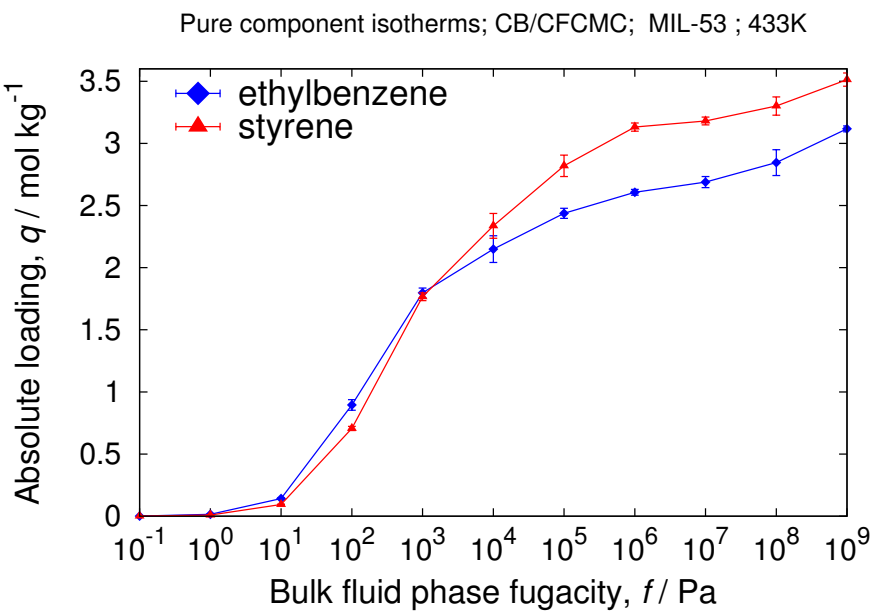

5.9 MIL-125

unit cell size	$a = 18.65430[\AA]$, $b = 18.65430[\AA]$,$c = 18.1444[\AA]$
unit cell angles	$\alpha = \beta = \gamma = 90[°]$
unit cells	$2 \times 2 \times 2$
framework density	[kg/m^3]
description	MIL-125
crystallographic data	ref. [32]
void fraction	0.620306 [-]
accessible pore volume	0.7542 [cm^3/g]
nitrogen surface area	2231.447617[m^2/g],1835.290387 [m^2/cm^3]
optimization	VASP fixed cell, PBE, precision=high
charges	REPEAT with PES from VASP

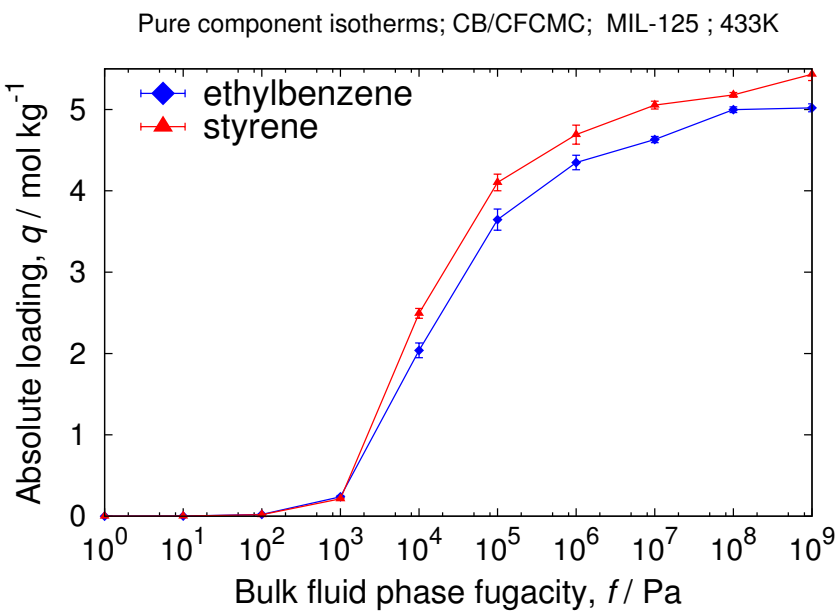

5.10 MIL-125-NH_2

unit cell size	$a = b = 18.729[\AA]$, $c = 18.172[\AA]$
unit cell angles	$\alpha = \beta = \gamma = 90[°]$
unit cells	$2 \times 2 \times 2$
framework density	861.6161 [kg/m^3]
description	MIL-125
crystallographic data	ref. [33]
void fraction	0.5921 [-]
accessible pore volume	0.6872 [cm^3/g]
nitrogen surface area	[m^2/g], [m^2/cm^3]
optimization	VASP fixed cell, PBE, precision=high
charges	REPEAT with PES from VASP

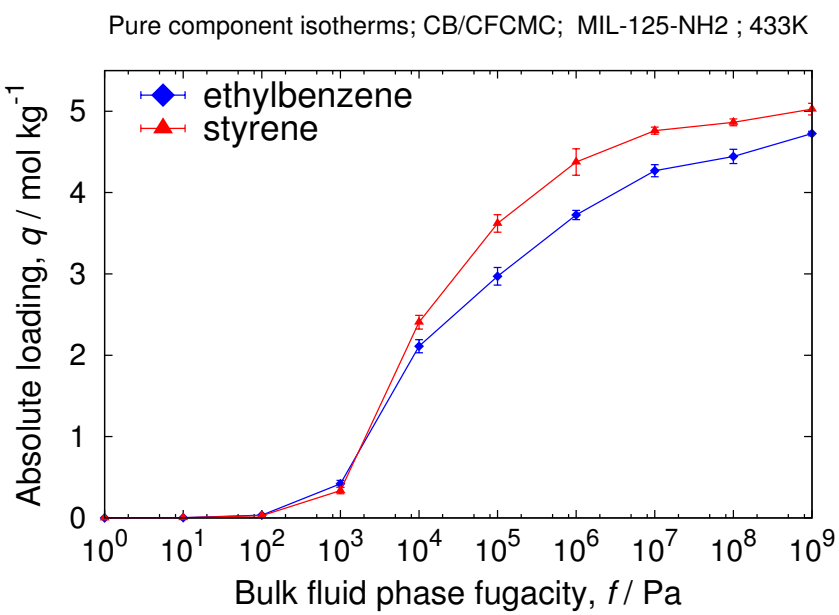

5.11 MOF-CJ3

unit cell size	$a = 20.588[\AA]$, $b = 20.588[\AA]$, $c = 17.832[\AA]$
unit cell angles	$\alpha = \beta = \gamma = 90[°]$
unit cells	$2 \times 2 \times 4$
framework density	954.2909 [kg/m^3]
description	MOF-CJ3
crystallographic data	ref. [34]
void fraction	0.4478[-]
accessible pore volume	0.3440 [cm^3/g]
nitrogen surface area	870 [m^2/g], 1133 [m^2/cm^3]
optimization	VASP fixed cell, PBE, precision=high
charges	REPEAT with PES from VASP

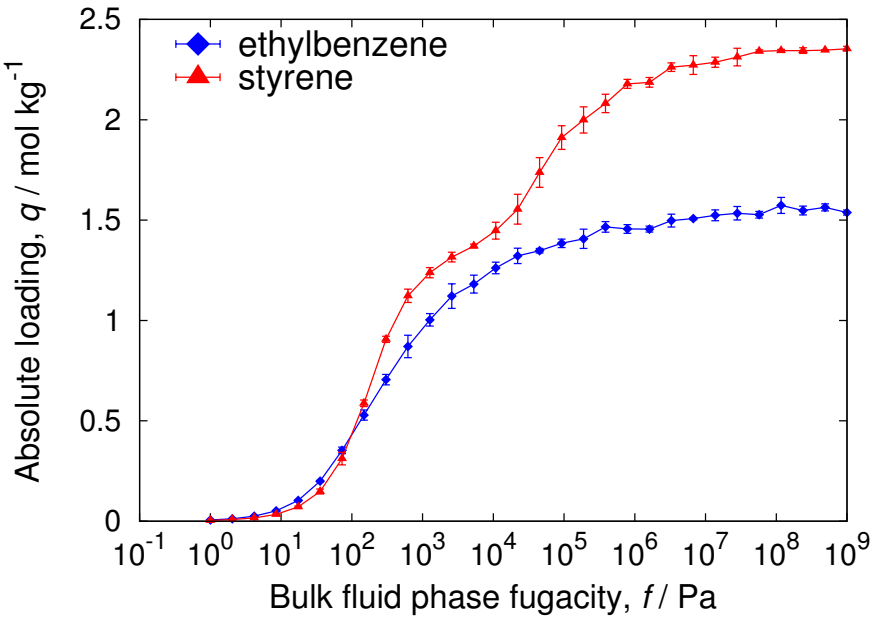

5.12 NiDOBDC

unit cell size	$a = 25.7856[\AA]$, $b = 25.7856[\AA]$, $c = 6.7701[\AA]$
unit cell angles	$\alpha = \beta = 90, \gamma = 120[°]$
unit cells	$2 \times 2 \times 4$
framework density	1194.120 [kg/m^3]
description	NiDOBDC
crystallographic data	ref. [35]
void fraction	0.6931[-]
accessible pore volume	0.5804 [cm^3/g]
nitrogen surface area	1311 [m^2/g], 1566 [m^2/cm^3]
optimization	-
charges	REPEAT with PES from VASP

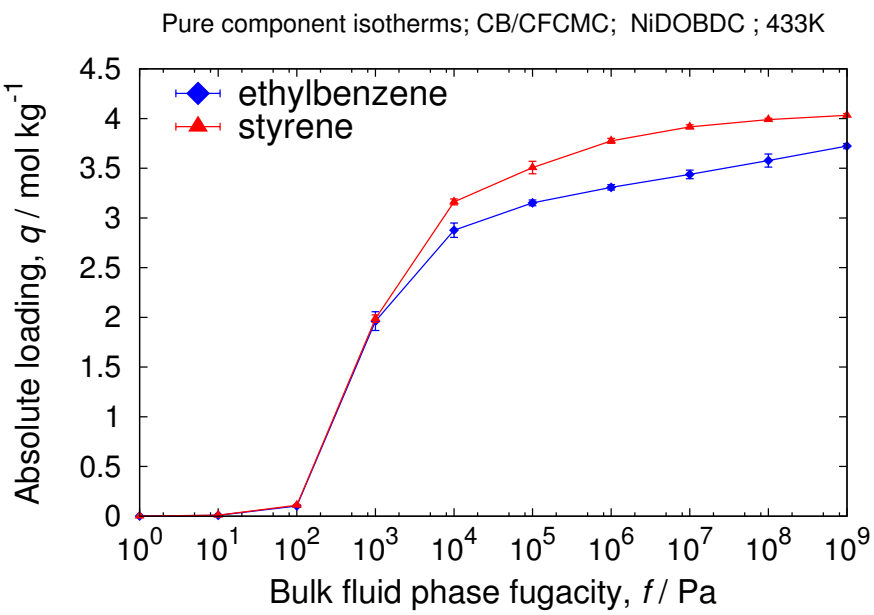

5.13 UiO-66

unit cell size	$a = b = c = 20.7004[\AA]$
unit cell angles	$\alpha = \beta = \gamma = 90[^\circ]$
unit cells	$2 \times 2 \times 2$
framework density	$1219.0883[kg/m^3]$
description	UiO-66
crystallographic data	ref. [36]
void fraction	0.496497 [-]
accessible pore volume	0.40718 $[cm^3/g]$
nitrogen surface area	1116 $[m^2/g]$, 1360 $[m^2/cm^3]$
optimization	-
charges	REPEAT with PES from VASP

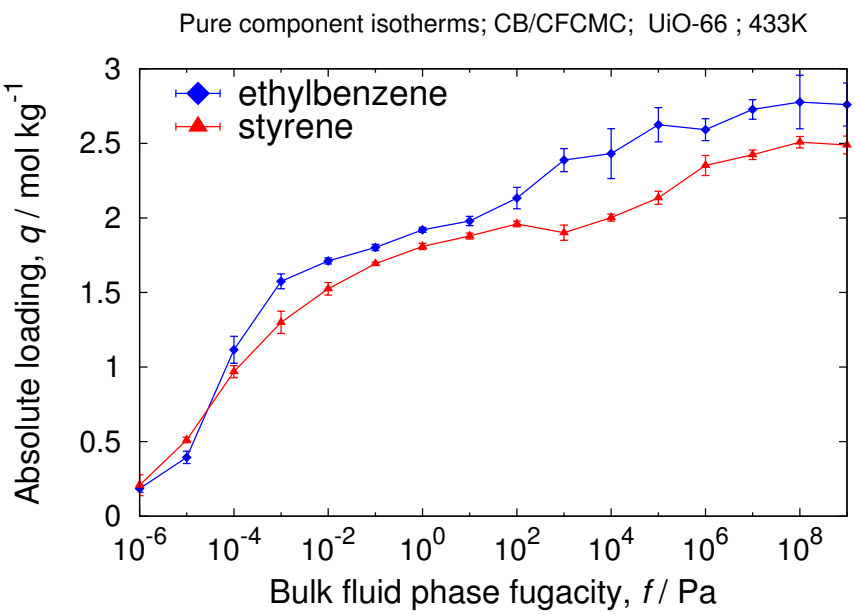

5.14 ZnDOBDC

unit cell size	$a = b = 25.9320[\AA]$, $c = 6.8365[\AA]$
unit cell angles	$\alpha = \beta = 90, \gamma = 120[°]$
unit cells	$2 \times 2 \times 4$
framework density	1219.604 [kg/m^3]
description	ZnDOBDC
crystallographic data	ref. [37]
void fraction	0.71931[-]
accessible pore volume	0.5898 [cm^3/g]
nitrogen surface area	1289 [m^2/g], 1572 [m^2/cm^3]
optimization	-
charges	REPEAT with PES from VASP

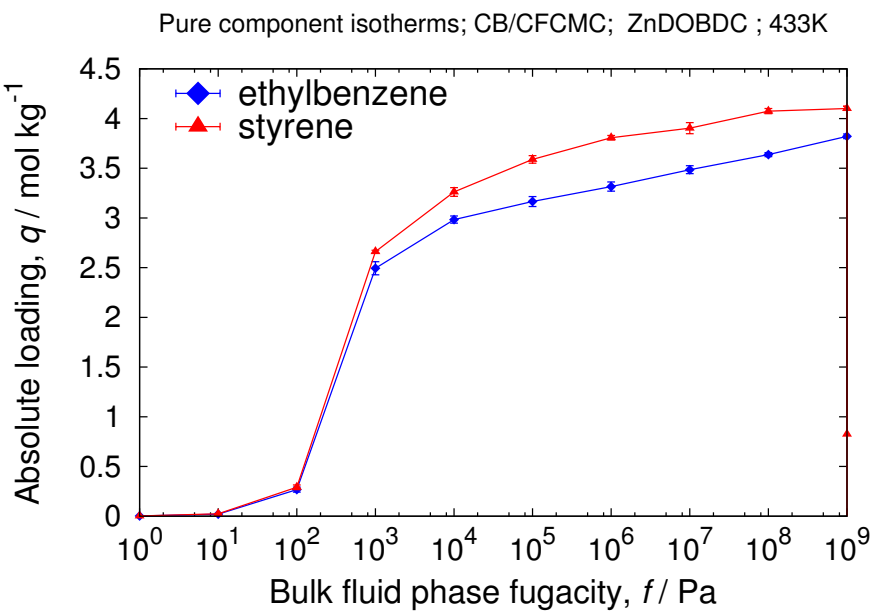

Bibliography

[1] Torres-Knoop, A.; Balaji, S. P.; Vlugt, T.; Dubbeldam, D. *J. Chem. Theory Comput* **2014**, *10*, 942–952.

[2] Siepmann, J. *Mol. Phys.* **1990**, *70*, 1145–1158.

[3] Siepmann, J.; Frenkel, D. *Mol. Phys.* **1992**, *75*, 59–70.

[4] Frenkel, D.; Mooij, G.; Smit, B. *J. Phys.: Condens. Matter* **1992**, *4*, 3053–3076.

[5] Shi, W.; Maginn, E. *J. Chem. Theory Comput.* **2007**, *3*, 1451–1463.

[6] Shi, W.; Maginn, E. *J. Comput. Chem.* **2008**, *29*, 2520–2530.

[7] Dubbeldam, D.; Knoop, A.; Walton, K. *Mol. Simulat.* **2013**, *39*, 1253–1292.

[8] Martin, M.; Siepmann, J. *J. Am. Chem. Soc.* **1997**, *119*, 8921–8924.

[9] Panagiotopoulos, A. *Int. J. Thermophys.* **1989**, *10*, 447–457.

[10] Qiu, S.; Pang, W.; Kessler, H.; Guth, J. *Zeolites* **1989**, *9*, 440–444.

[11] Newsam, J.; Treacy, M.; Koetsier, W. T.; de Gruyter, C. *Proc. Roy. Soc. A (London)* **1988**, *420*, 375–405.

[12] Wessels, T.; Baerlocher, C.; McCusker, L.; Creyghton, E. *J. Am. Chem. Soc.* **1999**, *121*, 6242–6247.

[13] Baerlocher, C.; McCusker, L.; Chiappetta, R. *Microporous Mater.* **1994**, *2*, 269–280.

[14] Galli, E. *Rend. Soc. Ital. Mineral. Petrol.* **1975**, *31*, 599–612.

[15] Olson, D.; Kokotailo, G.; Lawton, S.; Meier, W. *J. Phys. Chem.* **1981**, *85*, 2238–2243.

[16] van Koningsveld, H.; van Bekkum, H.; Jansen, J. *Acta Cryst. B* **1987**, *43*, 127–132.

[17] van Koningsveld, H.; Jansen, J. C.; ; van Bekkum, H. *Zeolites* **1990**, *10*, 235–242.

[18] van Koningsveld, H.; et al, *Acta. Cryst.* **1989**, *B45*, 423–431.

[19] Gramlich, V. *Ph.D. Thesis, ETH, Zürich, Switzerland* **1971**,

[20] Schlenker, J.; J.L.,; Rohrbaugh,; W.J.,; Chu,; P.,; Valyocsik,; E.W.,; Kokotailo, G. T. *Zeolites* **1985**, *5*, 355–358.

[21] Lobo, R.; van Koningsveld, H. *J. Am. Chem. Soc.* **2002**, *124*, 13222–13230.

[22] Fyfe, C.; Gies, H.; Kokotailo, G.; Marler, B.; ; Cox, D. *J. Phys. Chem.* **1990**, *94*, 3718–3721.

[23] Newsam, J. *J. Phys. Chem.* **1989**, *93*, 7689–7694.

[24] H.J. Choi, M. D.; Long, J. *J. Am. Chem. Soc.* **2008**, *130*, 7848–7850.

[25] Dietzel, P.; Morita, Y.; Blom, R.; Fjellvag, H. *Angew. Chem. Int. Ed* **2005**, *44*, 6354.

[26] Chui, S. S.-Y.; Lo, S. M.-F.; Charmant, J. P. H.; Orpen, A. G.; Williams, I. D. *Science* **1999**, *283*, 1148–1150.

[27] Li, H.; Eddaoudi, M.; O'Keeffe, M.; Yaghi, O. M. *Nature* **1999**, *402*, 276.

[28] Jin, Z.; Zhao, H.-Y.; Zhao, X.-J.; Fang, Q.-R.; Long, J.; Zhu, G.-S. *Chem. Comm* **2010**, *46*, 8612–8614.

[29] He, C.-T.; Tian, J.-Y.; Liu, S.-Y.; Ouyang, G.; Zhang, J.-P.; Chen, X.-M. *Chem. Sci.* **2013**, *4*, 351–356.

[30] Barthelet, K.; Marrot, J.; Riou, D.; Ferey, G. *Ang. Chem. Int. Ed.* **2002**, *41*, 281–284.

[31] Serre, C.; Millange, F.; Thouvenot, C.; Nogues, M.; Marsolier, G.; Louer, D.; Ferey, G. *J. Am. Chem. Soc.* **2002**, *124*, 13519–13526.

[32] Dan-Hardi, M.; Serre, C.; Frot, T.; Rozes, L.; Maurin, G.; Sanchez, C.; Ferey, G. *J. Am. Chem. Soc.* **2009**, *131*, 10857–10859.

[33] Fu, Y.; Sun, D.; Chen, Y.; Huang, R.; Ding, Z.; Fu, X.; Li, Z. *Angew. Chem. Int. Ed.* **2012**, *124*, 3420–3423.

[34] Fang, Z.; Zheng, S.; Tan, J.; Cai, S.; Fan, J.; Yan, X.; Zhang, W. *Journal of Chromatography A* **2013**, 132–8.

[35] Dietzel, P.; Panella, B.; Hirscher, M.; Blom, R.; Fjellvag, H. *Chem. Comm* **2006**, 959.

[36] Cavka, J.; Jakobsen, S.; Olsbye, U.; Guillou, N.; Lamberti, C.; Bordiga, S.; Lillerud, K. *J. Am. Chem. Soc.* **2008**, *130*, 13850–13851.

[37] Rowsell, J.; O.M.Yaghi, *J. Am. Chem. Soc* **2006**, *128*, 1304.